DOE/ET-53088-547 IFSR #547

Chaotic Transport by Rossby Waves in Shear Flow

DIEGO DEL-CASTILLO-NEGRETE
and
P.J. MORRISON
Institute for Fusion Studies
The University of Texas at Austin
Austin, Texas 78712

April 1992

Chaotic Transport by Rossby Waves in Shear Flow

Diego del-Castillo-Negrete and P.J. Morrison
Department of Physics and
Institute for Fusion Studies
The University of Texas at Austin
Austin, Texas 78712

Abstract

Transport and mixing properties of Rossby waves in shear flow are studied using Hamiltonian chaos theory. Attention is restricted to the case of shear flows with symmetric velocity profiles; the Bickley jet with velocity profile sech^2 is considered in detail. Motivated by linear stability analysis and experimental results, we propose a simple Hamiltonian model to study transport by waves in these shear flows. Chaotic transport, both for the general case and for the sech^2 profile, is investigated. The resonance overlap criterion is used to obtain an estimate for the destruction of barriers to transport and the notions of *banded* and *global* chaos are introduced to characterize the transport that typically occurs in symmetric shear flows. The role of potential vorticity conservation in chaotic transport is discussed. An area preserving map is obtained from the Hamiltonian model, that describes chaotic transport in a general symmetric shear flow. The map is shown to be a special case of a new map termed the *standard non-twist* map that exhibits, in addition to stochasticity, separatrix reconnection. The conclusions reached are used to explain experimental results on transport and mixing by Rossby waves in rotating fluids.

[*submitted to The Physics of Fluids A, April 1992.*]

PACS nos.: 47.35.+i, 05.45.+b, 51.10.y, 92.90.+x

I. Introduction

The goal of this work is to apply methods and ideas from Hamiltonian chaos theory to study transport properties of Rossby waves in shear flow. Attention is restricted to the case of symmetric shear flows of the form of zonal flows; in particular, the Bickley jet with the velocity profile $\propto \mathrm{sech}^2 y$ is considered in detail.

Zonal shear flows occur naturally in both the oceans and the atmosphere; two well-known examples are the Gulf stream and the polar night jet above Antarctica. Barotropic perturbations of these zonal flows produce Rossby waves [1] that have a crucial influence on transport and mixing, and an understanding of these transport properties is a major problem of Geophysical Fluid Dynamics. Needless to say, the real situation in the oceans and atmosphere is much more complicated than the simple model we are to present. However, as in many cases, a simplification of the real situation lends insight and gives rise to useful qualitative ideas.

Being two-dimensional and incompressible the flows we consider can be described by a stream function ψ. Hence, the Lagrangian trajectory $(x(t), y(t))$ of a fluid particle or of an advected passive scalar is described by the equations

$$\frac{dx}{dt} = -\frac{\partial \psi}{\partial y} \qquad \frac{dy}{dt} = \frac{\partial \psi}{\partial x} \,. \tag{1}$$

These equations are Hamilton's equations with the stream function identified as the Hamiltonian and the physical space (x, y) identified as the phase space (q, p). The form of Eqs. (1) makes it possible to study transport in two-dimensional incompressible hydrodynamics using the highly developed methods of Hamiltonian dynamics (see for example [2]). It is well-known that all time-independent one-degree-of-freedom Hamiltonian systems are integrable. Therefore in a fluid with a time-independent stream function all fluid particles move in a non-chaotic or integrable way, following the contours of constant ψ. When time dependence is added the Hamiltonian system is usually not integrable and so chaotic motion

is likely to appear, giving rise to what is referred to as chaotic advection or "Lagrangian turbulence" [3]–[6]. By chaotic transport we mean the transport that occurs when the fluid velocity field is not chaotic, but the fluid particle trajectories exhibit chaotic behavior. Regions of high mixing and transport in the fluid are identified with the chaotic regions of the associated Hamiltonian system, whereas barriers to transport are identified with integrable (non-chaotic) trajectories.

In Sec. II we review known results on propagation of Rossby waves in shear flows and consider the Bickley jet sech^2 velocity profile. Motivated by linear stability analysis, we propose a simple model for the stream function. Section III contains such a Hamiltonian model to study transport in general symmetric shear flows. After describing the phase space topology we apply the resonance overlap criterion [7], [8] to study the transport and mixing properties of the system. The terms *banded* and *global chaos* are introduced. Banded chaos accounts for the mixing that typically occurs in bands on each side of the zonal flow, whereas global chaos exists when there is no barrier to transport, a situation that typically does not occur. The role of potential vorticity conservation in chaotic transport is discussed. From the Hamiltonian system an area preserving map that describes chaotic transport in a general symmetric zonal flow is derived. In Sec. IV we apply the previous results to the special case of the Bickley jet. In Sec. V the model is used to explain qualitatively experimental results of Sommeria *et al.* [9], [10] concerning transport and mixing by Rossby waves in zonal flows in rotating fluids. Comparison of the model with previously proposed models [11], [12] is made. Section VI presents the conclusions. In Appendix A we introduce the *standard non-twist* map, a generic map that violates the twist condition. Properties of this map, e.g. separatrix reconnection and stochasticity, are also discussed and it is shown that the map defined in Sec. III and the traveling map [13] are both special cases of this new map.

II. A Model for the Stream Function

In order to study chaotic transport the stream function of the system is needed. In principle one should get this function by solving the Navier-Stokes equations with the appropriate boundary conditions. However, solutions of nonlinear fluid equations are difficult to obtain and so one has to resort to simplified approaches. One such approach is to use arguments based on linearization of the corresponding fluid equations. Within its limitations, linear theory is useful in that it sometimes gives simple ideas upon which a physically meaningful model for the stream can be constructed. On the other hand, experimental results can also be used to build a model. The goal in the present section is to obtain a simple model for the stream function that represents the propagation of Rossby waves in a shear flow, a model that is based on linear stability analysis [14], [15] and experimental results [9], [10].

In the study of Rossby waves one considers wave motion in a two-dimensional, incompressible, inviscid, rotating shallow water system where, in accordance with the beta plane approximation [1], the Coriolis force is assumed to depend linearly on one coordinate. A right-handed Cartesian coordinate system with z pointing in the direction of rotation and y in the direction of the Coriolis force gradient is adopted. That is, y points in the "northward" direction and x is a periodic coordinate in the "eastward" direction. In these coordinates an equilibrium shear or zonal flow has the form

$$\mathbf{v} = u_0(y)\,\hat{x}\ . \tag{2}$$

Upon introducing the stream function

$$\mathbf{v} = \hat{z} \times \nabla\psi \tag{3}$$

the velocity field becomes

$$u_0 = -\frac{\partial\psi_0}{\partial y}\ . \tag{4}$$

Here u_0 is assumed to be a symmetric function of y and so ψ_0 is antisymmetric. In the beta

plane approximation the potential vorticity is given by

$$q = \nabla^2\psi + \beta y \ , \tag{5}$$

where the parameter β is related to the gradient of the Coriolis force and the basic dynamics of the system is governed by the conservation of potential vorticity [1]:

$$\frac{\partial q}{\partial t} + (\mathbf{v}\cdot\nabla)q = 0 \ . \tag{6}$$

Let ψ_1 be a small perturbation of the zonal flow

$$\psi = \psi_0 + \psi_1 \tag{7}$$

and write

$$\psi_1 = \phi(y)e^{ik(x-ct)} \ . \tag{8}$$

Upon substituting (7) into (6) and linearizing, it is seen that $\phi(y)$ is a solution of the Rayleigh-Kuo equation,

$$(u_0 - c)\left[\frac{d^2\phi}{dy^2} - k^2\phi\right] + (\beta - u_0'')\phi = 0 \ , \tag{9}$$

with the appropriate boundary condition. Because u_0 is symmetric the eigenfunctions ϕ have definite parity. Only the eigenfunctions that produce symmetric or sinuous perturbations of the zonal flow are considered. Throughout the present work all variables are dimensionless, the velocity scale U is defined as the maximum zonal flow velocity and the length scale L measures the horizontal variation of the zonal flow. Hence, the dimensional variables are given by Ly, Uu, k/L, $(U/L^2)\beta$, etc. According to Eqs. (7) and (8), a general stream function that describes Rossby waves superimposed on an equilibrium zonal flow is given by

$$\psi = \psi_0 + \sum_j \phi_j \, e^{ik_j(x-c_j\,t)} \tag{10}$$

where ψ_0 is antisymmetric and the ϕ_i are symmetric eigensolutions of Eq. (9).

A critical layer of a zonal flow appears where the velocity c of a propagating wave matches the velocity u_0 of the zonal flow. One of the difficulties encountered in trying to solve Eq. (9) for a general profile is that the equation becomes singular at these critical layers. One way to approach this problem is to consider the effects of viscosity and/or nonlinearity in a critical layer, and then match the solutions inside and outside the layer. There is however the possibility of getting regular neutral wave [$\mathrm{Im}(c) = 0$] solutions of the Rayleigh-Kuo equation if it happens that $(\beta - u_0'')/(u_0 - c)$ remains finite when $c = u_0$. Kuo [14] has shown that the condition for the existence of such solutions is that the gradient of potential vorticity vanish at some point y^*

$$\beta - \frac{d^2 u_0}{dy^2}(y^*) = 0 \ , \tag{11}$$

where

$$c = u_0(y^*) \ . \tag{12}$$

These waves are marginal, that is, they represent a stability boundary in parameter space between unstable ($\mathrm{Im}(c) > 0$) and asymptotically stable ($\mathrm{Im}(c) < 0$) waves.

Therefore a zonal flow satisfying

$$\frac{d^2 u_0}{dy^2} - \beta = a(u_0 - c_1)(u_0 - c_2) \ , \tag{13}$$

where a is some constant and $u_{0\mathrm{min}} < c_{1,2} < u_{0\mathrm{max}}$, will be capable of supporting two neutral waves. A solution to this equation is given by

$$u_0 = \mathrm{sech}^2 y \tag{14}$$

with $a = -6$. This velocity profile is known as the *Bickley jet*. By construction, the potential vorticity of this profile is flat (i.e. $\partial q/\partial y = 0$) at points $\pm y_1^*$, and $\pm y_2^*$; it satisfies (11) and hence admits the two neutral waves. The phase velocities of these waves are given by [15]:

$$c_{1,2} = \frac{1}{3}(1 \pm \Delta) \ , \tag{15}$$

$$\Delta = \sqrt{1 - \frac{3}{2}\beta} \qquad \beta \in (0, 2/3) \,, \tag{16}$$

and the positions of the critical layers are given by

$$y^*_{1,2} = \mathrm{sech}^{-1}\sqrt{\frac{1 \pm \Delta}{3}} \,. \tag{17}$$

For $\beta = 2/3$ the velocities of the two waves merge to the value $1/3$ and the critical points coincide at $y^* = \mathrm{sech}^{-1}(1/\sqrt{3})$. When β tends to zero the velocity of the fast mode approaches the maximum value of $2/3$ and its critical points tend to $\mathrm{sech}^{-1}\left(\sqrt{2/3}\right)$, whereas the velocity of the slow mode goes to zero and its critical points tend to $\pm\infty$. For the velocity profile (14) the symmetric neutral solutions to the Rayleigh-Kuo equation are given by [15],

$$\phi(y) = \mathrm{sech}^2 y \tag{18}$$

$$k^2_{1,2} = 6c_{1,2} \,. \tag{19}$$

Between these marginally stable modes exists a band of unstable or growing modes with phase velocities and wavenumbers in the range $c_1 < \mathrm{Re}(c) < c_2$ and $k_1 < k < k_2$, respectively, for $0 < \beta < 2/3$. Since these unstable modes grow exponentially the linear calculation becomes invalid after some time. The system has finite energy and the growing process eventually stops because of nonlinear saturation effects, wave-zonal flow interaction and perhaps dissipation. Because the system is assumed periodic in the x-direction, the only allowed wavenumbers satisfy the wavelength quantization condition $m\lambda = D$, where λ is the wavelength, m an integer, and D the spatial period. We will say that a system is in its marginal state if the only modes that satisfy the quantization condition are the neutral modes. For an arbitrary change in the value of β the system is no longer at marginality. However, as the unstable modes grow the wave-zonal flow interaction can change the maximum velocity and width of the jet, so that the system relaxes to the marginal stable state and the growing process stops. In general, the barotropic instability tends to broaden and weaken a jet [1].

The relaxation of an eastward jet to marginal stability was observed experimentally by Sommeria *et al.* [10], who used this fact to explain the scaling relations of the maximum velocity and width of the jet.

Motivated by the preceding linear stability results and the experimental evidence of the relaxation to marginal stability, we propose as a model for the stream function a superposition of the zonal flow and the two neutral modes that exist at marginality

$$\psi = -\tanh y + \mathrm{sech}^2 y \sum_{i=1}^{2} \varepsilon_i \cos k_i(x - c_i t) , \tag{20}$$

where the c_i and k_i are given by Eqs. (15) and (19). This model for the stream function was originally proposed by the authors in [6]. Although in a real situation (e.g. the Sommeria *et al.* experiment [9], [10]) nonlinear effects may give rise to a more complicated stream function, the above simplified model will capture many of the transport properties of the system. Hamiltonian chaos, on which chaotic transport is based, is generic and depends only on the general topological properties of the phase space and on the range of frequencies of the waves perturbing the zonal flow.

III. Chaotic Transport in a General Symmetric Shear Flow

In the present section we discuss some general results on chaotic transport that depend only on the fact that the zonal flow and the perturbations (assumed small) are symmetric.

A. Phase space structure

Consistent with Eq. (10) is the following general Hamiltonian that models the motion of a passive scalar in a symmetric shear flow with Rossby waves:

$$H = H_0(y) + \sum_i \varepsilon_i \phi_i(y) \cos k_i(x - c_i t) , \tag{21}$$

where in this section H_0 is an arbitrary antisymmetric function and ϕ_i an arbitrary symmetric function. This Hamiltonian has the standard structure, possessing an integrable part H_0, that represents the zonal flow, and a nonintegrable small perturbation that represents the waves.

In order to characterize the phase space of this Hamiltonian in a simple way, only a single mode is considered. After canonically transforming to a frame co-moving with the wave, the single mode Hamiltonian H_i becomes,

$$H_i = H_0(y) + \varepsilon_i \, \phi_i(y) \cos(k_i \, x) + c_i \, y \ . \tag{22}$$

The fixed (stagnation) points $(\tilde{x}, \tilde{y})$ are solutions of the equations

$$\dot{x} = -\frac{dH_0}{dy} - \varepsilon_i \frac{d\phi_i}{dy} \cos(k_i \, x) - c_i = 0 \tag{23}$$

$$\dot{y} = -\varepsilon_i \, k_i \, \phi_i \sin \, k_i \, x = 0 \ . \tag{24}$$

In the case of interest $\phi_i > 0$ everywhere; therefore from Eq. (24)

$$\tilde{x}_i = \frac{n\pi}{k_i} \ , \qquad n = 0, 1, \ldots \tag{25}$$

and Eq. (23) becomes

$$\frac{dH_0}{dy} + (-1)^n \varepsilon_i \frac{d\phi_i}{dy} + c_i = 0 \ . \tag{26}$$

In general this is a transcendental equation for $\tilde{y}$ and cannot be solved explicitly. However, since ε_i is small, an approximate solution to first order in epsilon is given by

$$\tilde{y}_i \approx \tilde{y}_i^{(0)} + \varepsilon_i \, \tilde{y}_i^{(1)} \ . \tag{27}$$

Expanding H_0 and ϕ_i in Taylor series near $\tilde{y}_i^{(0)}$ yields

$$\tilde{y}_i = (-1)^n \left[y_i^* + \varepsilon_i \, A_i \right] \ , \tag{28}$$

where

$$A_i = -\frac{(d\phi_i/dy)_{y_i^*}}{(d^2H_0/dy^2)_{y_i^*}} \tag{29}$$

and y_i^* is the location of the critical layer (c.f. Eq. (12)). In a symmetric zonal flow d^2H_0/dy^2 is positive (negative) for y positive (negative), while on the other hand, for symmetric (sinuous) perturbations $d\phi_i/dy$ is negative (positive) for y positive (negative). Therefore A_i is always positive, and the fixed points are shifted a distance of order ϵ with respect to the critical layer.

The stability of a given fixed point is determined by linearizing the equations of motion. For Hamiltonian systems, if the eigenvalues of the matrix representing the linearized equations are real then the fixed point is hyperbolic (unstable), whereas if the eigenvalues are complex conjugates the fixed point is elliptic (neutrally stable). For a single degree-of-freedom Hamiltonian system the point $(\widetilde{x}, \widetilde{y})$ is elliptic if and only if

$$\left[\left(\frac{\partial^2 H}{\partial x^2}\right)\left(\frac{\partial^2 H}{\partial y^2}\right) - \left(\frac{\partial^2 H}{\partial x\,\partial y}\right)^2\right]_{(\widetilde{x},\widetilde{y})} > 0\ . \tag{30}$$

Upon substituting Eq. (22) into this condition it is seen that to first order in epsilon the fixed point is elliptic if and only if

$$(-1)^{n+1}\,\frac{d^2\,H_0}{dy^2}\,(\widetilde{y}_i) > 0\ . \tag{31}$$

Note that, at this order, the stability depends only on the sign of the zonal flow vorticity. Equations (25), (28), and (31) indicate that the phase space topology of the general Hamiltonian representing symmetric (sinuous) linear perturbation of a symmetric zonal flow is as shown in Fig. 1.

B. Resonance overlap

It is evident that with a single mode the Hamiltonian is time independent in the co-moving or wave frame and is thus integrable. However, perturbation of this integrable motion by a second mode will, in general, give rise to chaotic motion. A qualitative description of how the

presence of two modes generates chaotic trajectories is provided by the Chirikov resonance overlap criterion [7], [8]. Also, this criterion is useful for estimating the location and size of the chaotic regions.

For a Hamiltonian of the type (21) *resonances* y_i^* are defined as the places where the frequency of the perturbations matches the frequency of the unperturbed Hamiltonian,

$$-\frac{dH_0}{dy}(y_i^*) = c_i \ . \tag{32}$$

Comparison with Eq. (12) reveals that critical layers in fluid mechanics correspond exactly to resonances in the Hamiltonian model. Near a resonance the unperturbed phase space is distorted giving rise to an island chain with the width dependent upon the size of the perturbation. When two modes are present the resonances compete and chaos ensues. According to the overlap criterion, the last integrable trajectory or barrier between two resonances is destroyed when the sum of the half widths of the two resonance "islands" (calculated independently of one another) equals the distance between the resonances; that is,

$$\frac{W_1}{2} + \frac{W_2}{2} = \left| y_2^* - y_1^* \right| \ , \tag{33}$$

where W_1, W_2 are the widths of the islands and y_i^* is the position of the i^{th} resonance (see Fig. 2). Observe that according to the overlap criterion, barrier destruction depends not only on the strength of the perturbations (measured by W_i), but also on the frequencies of the perturbations. The latter is measured by the distance between the resonances. It is important to keep in mind that this is only a rough criterion, but it often yields good estimates for barrier destruction. The overlap criterion is easy to apply and provides a qualitative picture of the appearance of chaos in the phase space.

To compute the width of the resonances in a simple way it is useful to make the so-called "pendulum approximation." One begins with the Hamiltonian of the i-mode in its co-moving frame (Eq. (22)). Upon expanding around the resonance $y = y_i^* + p$ and using Eq. (32), the

Hamiltonian becomes for small p and ε,

$$H_i = \frac{1}{2}\,p^2 \left(\frac{d^2 H_0}{dy^2}\right)_{y_i^*} + \varepsilon_i\,\phi_i(y_i^*)\cos k_i\,x + \left[H_0(y_i^*) + c_i\,y_i^*\right] \;, \tag{34}$$

where the last term, being a constant, can be ignored. With the following definitions

$$\begin{aligned} m_i &= \left|\frac{d^2 H_0}{dy^2}\,(y_i^*)\right|^{-1} \\ \gamma_i &= \varepsilon_i\,\phi_i(y_i^*) \;, \end{aligned} \tag{35}$$

the Hamiltonian becomes

$$H_i = \frac{p^2}{2m_i} + \gamma_i \cos(k_i x) \;. \tag{36}$$

In this approximation, the width of the resonance is given simply by the distance between the pendulum separatrices

$$W_i = 4\sqrt{\gamma_i\,m_i} \;, \tag{37}$$

and the overlap criterion is given by

$$\sqrt{\varepsilon_1 \frac{\phi_1(y_1^*)}{|u_0'(y_1^*)|}} + \sqrt{\varepsilon_2 \frac{\phi_2(y_2^*)}{|u_0'(y_2^*)|}} = \frac{1}{2}\,|y_2^* - y_1^*| \;. \tag{38}$$

Depending on the width and relative positions of the resonances one can distinguish several cases of chaotic transport in the system. The first corresponds to the case where the resonances are far enough from each other so that no overlap occurs. In this case the vicinity of the line $y = 0$ will have invariant curves, and in addition there will be invariant curves separating y_1^* from y_2^* and $-y_1^*$ from $-y_2^*$ (see Fig. 2). Each of the resonances will have its own *stochastic layer*, but transport between the resonances will not occur (see for example Fig. 5(a)).

The next case corresponds to the situation when the resonance located at y_2^* overlaps that located at y_1^*, while both remain above the line $y = 0$, and because of symmetry, $-y_2^*$ will overlap $-y_1^*$ below $y = 0$. This overlap destroys the invariant curves between y_1^* and y_2^* (and simultaneously those between $-y_1^*$ and $-y_2^*$) resulting in symmetric bands of chaos

separated by a band of nearly integrable trajectories spanning the central region. We refer to this case as *banded chaos.* Because the phase space is two dimensional, the invariant tori of the nearly integrable region near $y = 0$ divides the phase space into two regions, precluding transport across the central region.

In the banded chaos regime there exist two different situations depending on the strength of the perturbations. For small perturbations there are finite regions of stability or "islands" around the primary elliptic fixed points (see for example Fig. 5(b)). These islands of stability correspond to the regions of trapped particles in the fluid and so we refer to this regime as *banded chaos with trapping regions.* For stronger perturbations the primary elliptic fixed points become unstable and the islands of stability are destroyed (see Fig. 5(c)). We refer to this case as *banded chaos without trapping regions.*

The last case is the extreme situation where the integrable trajectories near the line $y = 0$ are destroyed because of the overlap of resonances located above and below this region. Since all barriers that divide the phase space are destroyed, we refer to this case as *global chaos.* This might happen if, for example, the resonance at y_2^* overlaps with that at $-y_1^*$. Such overlap is degenerate since the resonance $-y_2^*$ must "pass through" resonance y_1^*, which destroys the validity of the isolated resonance picture upon which the overlap in criterion is based. Nevertheless, even in this degenerate case, the qualitative ideas obtained by applying the overlap criteria turn out to be useful (as will be seen in Sec. IV). The possibility of having this kind of overlap requires waves with phase velocities near the maximum zonal flow velocity. Physically the wave phase velocities must be less than the maximum zonal flow velocity, and for this reason global chaos is difficult to achieve.

C. Chaotic transport and potential vorticity conservation

In this subsection the issue of self-consistency between potential vorticity conservation and chaotic transport is addressed. If potential vorticity is conserved then advected particles

must follow the contours of constant q. Since the velocity field is assumed non-chaotic, contours of constant q evolve in a non-chaotic way; therefore, the fluid particles following these contours can not exhibit chaotic behavior. Thus we arrive at an apparent contradiction between the co-existence of chaos and potential vorticity conservation.

However, this "contradiction" does *not* exist if the potential vorticity is constant in some finite, two-dimensional spatial region. In such a region potential vorticity conservation and chaotic advection are consistent because fluid particles are able to mix chaotically while preserving their constant value of potential vorticity. For the model of Eq. (21) regions of chaotic advection coincide with regions where the potential vorticity is nearly constant. This is because Kuo's theorem [Eq. (11)] requires that neutral modes exist at places where $\partial q_0/\partial y = 0$. In the Hamiltonian picture the neutral modes create resonances and these are located in regions where the potential vorticity tends to be constant. If the resonances y_1^* and y_2^* (the same applies to $-y_1^*$ and $-y_2^*$) are close enough together, then the potential vorticity is nearly constant in the region between them. At the same time, the overlap criterion predicts chaotic motion in just this region. Thus we are naturally lead to expect that *regions of constant potential vorticity correspond to regions of mixing.* On the other hand, as discussed above, the overlap of resonances y_1^* and $-y_2^*$ (the same applies to y_2^* and $-y_1^*$) and thus the existence of global chaos is unlikely to occur. The region between y_1^* and $-y_2^*$ is a region where the zonal flow obtains its maximum value and also where the gradient in potential vorticity obtains its maximum. Thus we are naturally lead to expect that *gradients in potential vorticity correspond to barriers to transport.*

The above considerations are kinematical in the sense that the stream function, and hence the potential vorticity, have been assumed and are at-best solutions to only linear order. The next question one should address is, what is the dynamical mechanism by which potential vorticity is homogeneized in regions of the fluid. In essence this is the study of mixing and transport of vorticity, a complicated problem since potential vorticity is *not* a passive scalar

but, in a sense, provides its own stirring. Nevertheless, it is interesting that even though potential vorticity is not passively advected, there are cases where it mixes as if it were [16].

D. Area preserving maps

The use of Poincáre sections is by now a well-established and useful tool for studying chaos. However, if the differential equations are integrated directly, the number of points in such a plot can only be increased at the considerable cost of integration time, t; for example, to have N points $t = NT$, where T is the period of the perturbation. For statistical studies of particle motion (and hence transport), many orbits must be integrated for large values of t. For such studies it has proven advantageous to study, in lieu of the original Hamiltonian differential equations, an area preserving map. The simplest way to obtain this kind of map is to discretize the equations subject to the condition of area preservation. In fact the construction of the map for the integrable case, where there is shear flow but no wave contribution, is exact and straightforward:

$$x_{n+1} = x_n - \delta \frac{\partial H_0}{\partial y}(y_{n+1}) \tag{39}$$

$$y_{n+1} = y_n \ . \tag{40}$$

Here the constant δ is related to the discretization of time. To include the effect of the waves this "zonal flow map" is perturbed as follows:

$$x_{n+1} = x_n - \delta \frac{\partial H_0}{\partial y}(y_{n+1}) + f(x_n, y_{n+1}) \tag{41}$$

$$y_{n+1} = y_n + g(x_n, y_{n+1}) \ ; \tag{42}$$

to be area preserving [8]

$$\frac{\partial f}{\partial x_n} + \frac{\partial g}{\partial y_{n+1}} = 0 \ . \tag{43}$$

The explicit form of the functions f and g is determined by the equations of motion. When only a single mode is present, the equation of motion for the y coordinate in a frame co-

moving with the mode is given by

$$\frac{dy}{dt} = -\varepsilon k\, \phi(y) \sin kx \ . \tag{44}$$

Discretization of this equation gives,

$$g = -\varepsilon\delta k\, \phi(y_{n+1}) \sin kx_n \ , \tag{45}$$

while the function f can be obtained from the area preservation condition. Thus the following map is obtained:

$$x_{n+1} = x_n - \delta \frac{\partial H_0}{\partial y}(y_{n+1}) - \varepsilon\delta \frac{d\phi}{dy}(y_{n+1}) \cos kx_n \tag{46}$$

$$y_{n+1} = y_n - \varepsilon\delta\, k\, \phi(y_{n+1}) \sin kx_n \ . \tag{47}$$

This map is complicated by its implicit form; from the initial points x_n and y_n one first obtains y_{n+1} by solving Eq. (47) by, e.g. Newton's method, then with this value, x_{n+1} is obtained from Eq. (46). However, an explicit map can be obtained by expanding the functions H_0 and ϕ near $y = 0$,

$$x_{n+1} = x_n + a(1 - y_{n+1}^2) \tag{48}$$

$$y_{n+1} = y_n - b \sin\, x_n \ , \tag{49}$$

where the variables x, y have been scaled by k and $\sqrt{|u''(0)|/2}$, respectively, and the parameters a and b are given by

$$a = \delta k \qquad b = \varepsilon\delta k \phi(0) \sqrt{|u''(0)|/2} \ . \tag{50}$$

This map is a special case of a new map that we called the *standard non-twist* map which is described below and in the Appendix A.

The discretization process, upon which the derivation of the map is based, assumes $\delta \ll 1$. Also note the value of ε is assumed to be small. For parameter values satisfying these two

conditions, the map provides a remarkably good approximation to the Hamiltonian system defined by (22). This can be seen by comparing Fig. 1 with the iterations of the map for $a = 0.5$ and $b = 0.125$ shown in Fig. 3. When the values of a and b are increased the map exhibits stochasticity that does not occur in the single wave Hamiltonian system of (22). To understand the origin of this stochasticity, and the relationship with the chaotic behavior of the two wave Hamiltonian system of Eq. (21), observe that if x_n and y_n denote $x(t)$ and $y(t)$ just before the time $t = n$, then the discrete map of (48) and (49) can be obtained by direct integration of the following equations:

$$\frac{dx}{dt} = a(1 - y^2)$$

$$\frac{dy}{dt} = -b \sin x \sum_{m=-\infty}^{\infty} \delta(t - m) \; . \tag{51}$$

The Hamiltonian for these equations is given by

$$H = -ay + \frac{a}{3}y^3 + b \sum_{m=-\infty}^{\infty} \cos(x - 2\pi m t) \; , \tag{52}$$

where the Fourier representation of the periodic delta function has been used. From here it is seen that the effect of the discretization is to perturb the zonal flow with an infinite number of waves . Each one of these waves will create a resonance located at

$$y_m^{\pm} = \pm\sqrt{1 + \frac{2\pi m}{a}} \; . \tag{53}$$

Note that the position of the $m = 0$ resonance is always $y = \pm 1$, whereas the positions of the other resonances depend on the value of $a = \delta k$. In accordance with the overlap criterion, the stochasticity in the map is due to the overlap of these resonances. For small values of δ all the resonances with $m \geq 1$ are located far from the $m = 0$ resonance and therefore the motion near this resonance does not exhibit chaos. This explains the high degree of integrability of the map in situations when $a, b \ll 1$ [c.f. Fig. 3]. When the values of a and b are increased, the resonances approach each other and chaos ensues. Although the

Hamiltonian (52) contains an infinite number of resonances, the stochasticity near $y = 0$ [where the map (48) and (49) is a valid model] is mostly due to the resonances closest to this region. We can say that the stochastic behavior near $y = 0$ is caused by the overlap of the $m = 0$ and the $m = 1$ resonances. In this respect the stochasticity in the map is similar to the stochasticity of the original Hamiltonian (21), where chaotic motion arises as a result of the resonance overlap of the two modes. However this analogy is not perfect since the $m = 0$ and $m = 1$ modes in the map have identical wave numbers, whereas in the Hamiltonian (21) the overlapping modes have in general different wave numbers.

The stochasticity of the map of (48) and (49) can be studied quantitatively by approximating it locally by the standard map [8]. Writing $y = y_0^+ + p$, the map in neighborhood of the $m = 0$ resonance, reduces to

$$x_{n+1} = x_n - p_{n+1}$$

$$p_{n+1} = p_n - \kappa \sin x_n \ , \tag{54}$$

which is the standard map with $\kappa = 2ab$. For the standard map, the onset of widespread stochasticity occurs when κ approaches a threshold of approximately one; therefore the threshold for the $m = 0$ resonances is given by $ab = 1/2$. This result explains the high degree of integrability of the map, as observed in Fig. 3, since there $\kappa = 0.125$.

In Sec. IV we consider the specific case of the Bickley jet; it is seen that indeed the iterations of the area preserving map reproduce qualitatively the behavior obtained by numerically integrating Hamilton's equations.

For the standard non-twist map mentioned above a and b are arbitrary independent parameters; i.e., not necessarily given by (50). In the Appendix A we study the standard non-twist map and show that it has a very rich structure exhibiting in addition to stochasticity, separatrix reconnection; i.e., topological rearrangement of level curves. Upon setting in this map $a = b$ the traveling wave map [13] is obtained as a special case.

A common and interesting property of these maps is that they violate the so-called twist condition: a general map of the form (41) and (42) satisfies the twist condition provided the function $\partial H_0/\partial y$ is a monotonic function of y; that is $\partial^2 H_0/\partial y^2 \neq 0$ for all y. However in the cases of interest in this paper $\partial H_0/\partial y$ represents the zonal flow velocity that generically has a maximum: hence, $\partial^2 H_0/\partial y^2 = 0$, at $y = 0$. Since most results regarding area preserving maps require the twist condition, the consequence on transport and stochasticity upon violation are not well-understood and deserve further investigation.

For a given symmetric shear flow we know u_0 and once the function ϕ is known, the map of (48) and (49) allows us to study the transport properties of the flow in the vicinity of the center of the zonal flow. In the next section we will see this in detail when we apply the map to the Bickley jet.

IV. Chaotic Transport in the Bickley Jet

As an illustration of the general ideas explained above, the specific case of chaotic advection by Rossby waves in the Bickley jet is now considered. From Eqs. (18) and (21) the model Hamiltonian in this case is

$$H = -\tanh\, y + \varepsilon_2\, \mathrm{sech}^2 y \cos k_2 x + c_2 y + \varepsilon_1\, \mathrm{sech}^2 y \cos(k_1 x - \Omega t)\ , \tag{55}$$

where we have canonically transformed to the co-moving frame of the slower wave and $\Omega \equiv k_1(c_1 - c_2)$ with c_i and k_i given by Eqs. (15) and (19). The Hamiltonian for a single wave in its co-moving frame is given by

$$H_i = -\tanh\, y + \varepsilon_i\, \mathrm{sech}^2 y \cos k_i x + c_i y\ . \tag{56}$$

Using (25) and (28) the fixed points are seen to be

$$\widetilde{x}_i = \frac{n\pi}{k_i}\ ; \qquad n = 0, 1, \ldots \tag{57}$$

$$\widetilde{y}_i = (-1)^n \left[y_i^* + \varepsilon_i \right]\ , \tag{58}$$

where y_i^* is determined by Eq. (17). For $\beta = 2/3$ the fixed points of both modes coincide at $\tilde{y} = (-1)^n \left[\text{sech}^{-1}(1/\sqrt{3}) + \varepsilon_i\right]$. When β tends to zero the fixed points of the fast (first) mode tend to their minimum value $\tilde{y}_1 = (-1)^n \left[\text{sech}^{-1}\left(\sqrt{2/3}\right) + \varepsilon_i\right]$, whereas the fixed points of the slow (second) mode tend to infinity $\tilde{y}_2 \to \pm\infty$. Equation (31) implies that $(\tilde{x}_i, \tilde{y}_i)$ is stable if and only if

$$(-1)^{n+1} \tanh(\tilde{y}_i) > 0 \ . \tag{59}$$

Therefore, for n even (odd) the fixed points are shifted upwards (downwards) a distance ϵ from the critical line $[u_0(y^*) = c]$ and for n even (odd) the fixed points above $y = 0$ become hyperbolic (elliptic) while those below become elliptic (hyperbolic), as shown in Fig. 1.

Now the pendulum approximation (36) is applied to the Hamiltonian of (56). Using Eqs. (37) and (17) the width of the resonances and their separation are given, respectively, by

$$W_i = \frac{2\sqrt{2\varepsilon_i}}{(1 - c_i)^{1/4}} \tag{60}$$

and

$$d_\pm = \left|y_2^* - y_1^*\right|_\pm = \left|\left|\text{sech}^{-1}\sqrt{c_1}\right| \pm \left|\text{sech}^{-1}\sqrt{c_2}\right|\right| \ . \tag{61}$$

Therefore, the overlap criterion is given by the following:

$$\Lambda_\pm = \frac{\sqrt{2\varepsilon_1}}{(1 - c_1)^{1/4}} + \frac{\sqrt{2\varepsilon_2}}{(1 - c_2)^{1/4}} - \left|\left|\text{sech}^{-1}\sqrt{c_1}\right| \pm \left|\text{sech}^{-1}\sqrt{c_2}\right|\right| = 0 \ , \tag{62}$$

where the $-(+)$ sign corresponds to banded (global) chaos. (This was previously given in [6].) Negative (positive) values of $\Lambda_\pm$ correspond to non-overlapping (overlapping) values of β. The dependence of the width on β is weak; however, the distance between resonances depends strongly on β. Figure 4 shows the distance as a function of β. The existence of a nonzero minimum value of d_+ implies that global chaos cannot exist for small values of ε_i. That is, for any value of β, the resonances that would generate global chaos are always separated by a finite distance, and therefore never overlap for small values of ε_i. On the

other hand, the distance between the resonances on each side of the jet is small for beta near 2/3, therefore banded chaos is expected for small values of ε_i.

The above conclusions can be restated in terms of the phase velocities c_i, since these quantities determine the positions of the resonances. The closer a resonance is to the center of the jet, the larger the corresponding phase velocity. Therefore, since the dispersion relation requires the phase velocities to lie in the range $0 < c_i < 2/3$, where unity corresponds to the maximum jet velocity, the resonances can not be arbitrarily close to the center and hence, global chaos is not expected to exist. On the other hand, because at marginality the difference between the phase velocities of the two waves is small, the resonances at each side of the jet are close together and so banded chaos is expected to occur. Below these conclusions are substantiated by numerical examples.

Since the system is assumed to be periodic in the x-direction the wavelength quantization condition requires $m_1\,\lambda_1 = m_2\,\lambda_2 = D$, where λ_i are the wavelengths, m_i the mode numbers, and D is the total length of the system in the x-direction. Figure 5(a) shows a Poincáre section for the Hamiltonian (55) with $\varepsilon_1 = 0.1$, $\varepsilon_2 = 0.3$, and $\beta = 0.186$ that gives according to (15) and (19) $c_1 = 0.616$, $c_2 = 0.05$, $k_1 = 1.922$, and $k_2 = 0.548$. Here $m_1 = 7$ and $m_2 = 2$ and, accordingly, $D = 22.9$. For clearer visualization only points with $x \in (0, D/2)$ were plotted. For the chosen value of β, $0 > \Lambda_+ = -1.55$; therefore, according to the criterion of Eq. (62) global chaos should not be present. The existence of the invariant curves in the region $y \in (-0.5, 0.5)$ verify numerically this fact. On the other hand, the invariant curves starting in the neighborhood of $x = 0, y = 2.1$, and $y = -0.9$ indicate that banded chaos is also not present because these integrable trajectories separate the resonances. This fact is also in agreement with Eq. (62); since $0 > \Lambda_- = -0.10$ the resonances are not close enough to destroy all of the invariant curves between them.

Figure 5(b) is a Poincáre section for the same values of ε_i but for $\beta = 0.317$. Hence, $c_1 = 0.575, c_2 = 0.092, k_1 = 1.857$, and $k_2 = 0.743$. In this case $m_1 = 5$ and $m_2 = 2$ and so

$D = 16.92$. Again for simplicity only $x \in (0, D/2)$ is shown. As in the previous case the central integrable trajectories indicate that global chaos is not present, in agreement with Eq. (62), which gives $0 > \Lambda_+ = -1.29$. However, in this case the resonances located above and below the line $y = 0$ are close enough together so that the invariant curves between them are destroyed, in agreement with the criterion, which gives $0 < \Lambda_- = 0.26$. The presence of stability islands around the primary elliptic fixed points indicate that we have banded chaos with trapping regions.

Figure 5(c) shows the extreme case of $\beta = 0.614$ (same values of ε_i), $c_1 = 0.427, c_2 = 0.240, k_1 = 1.6, k_2 = 1.2, D = 15.7, m_1 = 4$, and $m_2 = 3$. In this case $0 > \Lambda_+ = -0.99$ and $0 < \Lambda_- = 0.99$. The Poincáre section exhibits banded chaos without trapping regions and the absence of global chaos, as expected. In this extreme case the resonances are close enough together to destroy the stability islands observed in Fig. 5(b). This fact has important consequences on the transport properties of the flow, since the islands represent regions of trapped particles.

For large enough values of β and ε_i global chaos can be produced. Numerically global chaos is observed for $\varepsilon_1 = 0.5$, $\varepsilon_2 = 0.5$, and $\beta = 0.614$. However, it is important to note that our model, based on the superposition of linear waves, assumes that the values of ε_i are small. Also, the pendulum approximation used to derive Eq. (62) assumes small values ε_i. The breakup of the central barrier can only be archived at the expense of a strong violation of the conservation potential vorticity.

To shed light on the consistency problem between potential vorticity conservation and chaotic transport, we have plotted in Fig. 6 the zonal flow potential vorticity

$$q_0 = 2\,\mathrm{sech}^2 y \tanh y + \beta y \ ,$$

for $\beta = 0.614$, the same value used for Fig. 5(c). The plot reveals two regions where the potential vorticity is flat. Particles in these regions have, to first order, the same value of q_0 and thus can mix chaotically. This is indeed observed in the Poincáre section of Fig. 5(c),

where bands of chaos are located above and below the central barrier at approximately the places where q_0 is constant. At the same time, the existence of the central invariant barriers is related to the sharp gradient of potential vorticity at $y = 0$.

Now consider the map derived in Sec. III. For the specific case of the Bickley jet, the parameters of Eq. (50) for the map are given by

$$a = \delta k \qquad b = \varepsilon \delta k. \tag{63}$$

Choosing $\varepsilon = 1/4$, consistent with the requirement that ε be small, the map of Eqs. (48) and (49) becomes

$$x_{n+1} = x_n + a(1 - y_{n+1}^2) \tag{64}$$

$$y_{n+1} = y_n - \frac{a}{4} \sin x_n \ . \tag{65}$$

In Fig. 7(a) iterations of this map are plotted for $a = 1.5$. Observe that the map exhibits regions of banded chaos with trapping regions. In Fig. 7(b) the value of $a = 2.8$. Here the primary islands of stability are destroyed and the map exhibits banded chaos without trapping regions. Comparison of the plots of Fig. 5 and Fig. 7 shows that the map qualitatively reproduces the correct topology and stochastic behavior of the Hamiltonian system of (55).

V. Application of the Model to Experiment

In this section the model presented above is used to interpret results on transport and mixing in the rotating annulus experiments of Sommeria *et al.* [9], [10] (hereafter SMS) and more recently Solomon *et al.* [17]. The experiments are performed in an annular tank with a flat top and conical bottom that models the variation of the Coriolis parameter with latitude (see Fig. 8). The entire tank rotates rigidly. A co-rotating or "eastward" jet is generated by the action of the Coriolis force on water pumped radially inward from a set

of six outlets, located on the tank bottom at a common radius, to a set of six inlets also located on the bottom but at a smaller radius. At large enough pumping rates Rossby waves are observed to propagate eastward in the frame co-rotating with the tank. To elucidate the dynamics and transport SMS diagnose the experiment with particle streak photographs and dye visualization. Figure 9(a) shows an experimental contour plot of the stream function obtained from a particle streak photograph [11].

Recently two models have been proposed to study the dynamics and transport observed in this experiment. Behringer *et al.* [11] proposed an *ad hoc* model of the stream function motivated by experimental data. Numerical integration of the equations of motion showed qualitative agreement with the experimental results. The authors of [11] observed that in their model at least three waves are needed to break the central barrier to transport; i.e. two waves are insufficient for global transport. However, this conclusion is not correct in general. In their model two waves break the central barrier provided the appropriate values of the amplitudes and phase velocities are chosen. These values are predicted by the overlap criterion. Behringer *et al.* concentrated mostly on the wave amplitudes to study the breakup of the central barrier, but the frequencies of the waves also plays a crucial role. In [12], Polvani and Touma modeled the system using linear contour dynamics. Chaotic mixing was shown to exist on both sides of the jet when several waves are present. However, it was argued that transport across the jet can only take place through the nonlinear wave breaking of the jet itself.

Precise modeling of the SMS experiments is a difficult problem. These experiments were conducted at high Reynolds numbers and therefore a precise model would require the solution of the Navier-Stokes equations with forcing. Here, however, we are more interested in the transport properties of the flow than in the exact behavior of the velocity field. Because Hamiltonian chaos exhibits generic features, transport properties of the system should not depend critically on the exact form of the stream function but only upon its topology.

Therefore, we expect transport can be described by a simple model.

The previous sections dealt with Rossby waves propagating on shear flow in rectangular geometry, described by the Cartesian coordinates (x, y), whereas in the SMS experiments Rossby waves propagate in an annular region described by the polar coordinates (r, θ). For small jet widths and wavelengths, curvature effects of the annulus may be neglected and the results for Rossby waves propagating in the rectangular geometry can be applied to the annulus. A direct way of doing this "slab" approximation is by simply writing $y = r_0 - r$ and $x = r_0\theta$, where r_0 is the radius of the maximum jet velocity. Accordingly, Eqs. (1) and (55) imply the following Hamiltonian:

$$\dot{r} = -\frac{\partial H}{\partial \theta} \; ; \qquad \dot{\theta} = \frac{\partial H}{\partial r} \tag{66}$$

$$H = \frac{AL}{r_0} \tanh\left(\frac{r - r_0}{L}\right) + \frac{AL}{r_0} \operatorname{sech}^2\left(\frac{r - r_0}{L}\right) \times \{\varepsilon_1 \cos(m_1\theta - \Omega t) + \varepsilon_2 \cos m_2\theta\} - \left(\frac{\omega_2}{m_2}\right) r \tag{67}$$

where

$$m_i = r_0 k_i / L \qquad \omega_i = k_i c_i (A/L) \tag{68}$$

$$\Omega = \frac{m_2\omega_1 - m_1\omega_2}{m_2}$$

with the dimensionless k_i and c_i given by Eqs. (19) and (15).

In this model A, L and r_0 are free parameters representing the maximum velocity, width and mean position of the zonal flow jet. Before discussing transport, consider now some comparisons of this model with the experimentally measured velocity field. SMS observed that the azimuthal average of the azimuthal component of the velocity field fits well a sech^2 profile. The azimuthal average of v_θ of the above model in the annulus rest frame yields

$$\langle u_\theta \rangle_\theta = A \operatorname{sech}^2\left(\frac{r - r_0}{L}\right) . \tag{69}$$

Hence, the zonal flow of the model is consistent with the experiment. Comparison of (69) with experimental results, gives numerical values for the parameters A, L and r_0. Typical values are $r_0 = 25\,\text{cm}$, $L = 6.4\,\text{cm}$ and $A = 12\,\text{cm/sec}$. These values will be used for comparison of the model with the experiment. Another experimental fact is that the eastward jet relaxes to a state near marginal stability, that is, the width of the jet and its maximum velocity adjust so that the dimensionless beta parameter is close to the value 2/3. Taking $\beta = 0.64$ yields from (68) $m_1 = 6$, $m_2 = 5$, $\omega_1 = 1.162\,\text{rad/sec}$ and $\omega_2 = 0.632\,\text{rad/sec}$. These values are in the range typically observed in the experiment, and will be used below. A more detailed comparison between the model and the experiment can be found in [6].

Figure 9(b) shows a plot of the phase space topology; i.e. contours of the Hamiltonian (67) at a fixed time, with $\varepsilon_1 = 0.1$ and $\varepsilon_2 = 0.3$. Comparison of this plot with the experimental stream function (Fig. 9(a)) shows reasonable qualitative agreement.

Figure 10(a) shows a Poincáre section for the model Hamiltonian of Eq. (63) for $\beta = 0.64$, $\varepsilon_1 = 0.1$, and $\varepsilon_2 = 0.3$. For these parameter values the overlap criterion gives $0 < \Lambda_- = 1.10$ for banded chaos and $0 > \Lambda_+ = -0.97$ for global chaos, which is consistent with the plot that shows the existence of banded chaos on both sides of the jet and a barrier to transport represented by the integrable wavy trajectories near the middle of the annulus. This pattern of chaotic mixing was observed in the SMS experiment when dye was injected in the outer (or inner) part of annulus.

Recent experiments conducted in the rotating annulus by Solomon *et al.* [17] have shown that under certain conditions trapping regions exist in the system. These experiments showed that dye injected in the outer part of the annulus mixes well on the injected side except for spots or islands where dye does not enter. Particle tracking with a video camera co-rotating with the tank has shown that, indeed, in these regions particles are trapped. These trapping regions are imbedded in the chaotic mixing region where the particles wander freely. Figure 10(b) illustrates this situation in the model. The Poincáre section was made with

the same parameters as those of Fig. 9(a), except $\varepsilon_1 = 0.03$. The plot shows banded chaos with trapping regions represented by the stable islands surrounding the primary elliptic fixed points.

VI. Conclusions

Methods from Hamiltonian chaos theory have been used to study transport by Rossby waves in symmetric shear flow. Motivated by linear stability analysis and experimental results a simple model stream function (Hamiltonian) was proposed. Chaotic transport properties of Rossby waves in a general symmetric shear flow were studied using the Chirikov resonance overlap criterion. The term banded chaos was introduced to describe the chaotic transport that occurs in bands located on each side of the maximum velocity of zonal flow, with the region of the maximum acting as a central barrier. Depending on the perturbations, banded chaos may or may not exhibit regions of trapped particles. The term global chaos was used to describe the case where the resonances overlap in such a way as to break the central barrier, a situation that typically does not occur. The consistency between chaotic transport and potential vorticity conservation was discussed, and it was argued that the chaotic transport takes place in regions where the potential vorticity tends to be constant.

From the Hamiltonian an area preserving map (that violates the twist condition) was obtained. For parameter values consistent with the model, the map was shown to reproduce correctly both the topology and the stochastic properties of the Hamiltonian. This map and also the traveling wave map of [13] were shown to be special cases of the standard non-twist map introduced and studied in Appendix A.

In Sec. IV we applied the previous results to the specific case of a sech^2 velocity profile. Poincáre sections constructed by numerical integration of the equations of motion showed good agreement with predictions based on the resonance overlap criterion. It was shown for this specific case how chaotic regions appear where the potential vorticity tends to be

constant and that barriers to transport appear where the gradients of potential vorticity are large.

Finally, the model was used to explain results on transport and mixing in the rotating annulus experiments of [9], [10], and [17]. Qualitative agreement was seen between the model and the experiment. Also, transport and mixing observed in the experiments appears to be well described by the model, which exhibits in accordance with the overlap criterion, high mixing on the sides of the jet (banded chaos) and no transport across the jet (global chaos).

We mention in closing that the model stream function (20) and the overlap criterion (62) presented here have recently been used to study transport and mixing in the Gulf Stream [18].

Acknowledgment

The authors acknowledge many fruitful conversations with W. Holloway, S. Meyers, T. Solomon, and H. Swinney, and thank them for sharing their experimental results. DdCN acknowledges support by the Instituto de Ciencias Nucleares Universidad Nacional Autonoma de Mexico. This work was supported by U.S. Dept. of Energy Contract No. DE-FG05-80ET-53088.

Appendix A –The Standard Non-twist Map

Here we introduce the standard non-twist map:

$$x_{n+1} = x_n + a(1 - y_{n+1}^2)$$

$$y_{n+1} = y_n - b \sin x_n \ , \tag{A1}$$

where a and b are arbitrary independent parameters. The x coordinate is assumed to be 2π-periodic. Hence, it is sufficient to consider values of a in the range $(0, 2\pi)$, because if $a > 2\pi$ x and y can be rescaled to produce an equivalent map with $a < 2\pi$. Since $\partial x_{n+1}/\partial y_{n+1} = 1$ at $y = 0$, this map violates the twist condition . According to Eq.(50), the map used to model transport by waves in a general symmetric shear flow is an special case of this standard non-twist map. In particular, taking $b = a/4$ yields the map for the Bickley jet of Eqs. (64) and (65). Also, by setting $b = a$ the traveling wave map of [13] is obtained. In addition to being relevant for studying transport in two dimensional hydrodynamics, the standard non-twist map is interesting in its own right, since it is a generic map that violates the twist condition and has a very rich behavior exhibiting both stochasticity and separatrix reconnection. Separatrix reconnection is a global bifurcation where the hyperbolic fixed points reconnect in topological different ways. Separatrix reconnection was observed by Howard and Hohs [19] in the logistic twist map.

In the remainder of this appendix we discuss briefly the reconnection properties of the standard non-twist map. As a first step, consider the period-one fixed points, which are located symmetrically with respect to the line $y = 0$

$$x = 0, \pi \qquad y_m^{\pm} = \pm\sqrt{1 + \frac{2\pi m}{a}} \quad m = 0, 1, \ldots \tag{A2}$$

Reconnection takes place between the primary islands of the $m = 0$ period-one fixed points. To derive a reconnection threshold, first approximate the map in the vicinity of a fixed point

by a Hamiltonian system, with Hamiltonian

$$H = -ay + \frac{a}{3}y^3 + b\cos x - 2\pi m y \ . \tag{A3}$$

In the system defined by Eq. (A3) reconnection occurs when

$$H(x = 0, y = y_0^+) = H(x = \pi, y = y_0^-) \ .$$

After substituting Eqs. (A2) and (A3) into this condition, the following reconnection threshold is obtained:

$$b = \frac{2}{3}a \ . \tag{A4}$$

When $b < 2a/3$ the map exhibits an heteroclinic type topology, whereas for parameter values satisfying $b > 2a/3$ the map possesses an homoclinic type topology. Figure (11) shows iterations of the map for three different values of parameters a and b. In Fig. (11 (a)) $a = 0.5$ and $b = 0.1$. Consistent with the previous results, the map exhibits the heteroclinic topology. In Figure (11 (b)) the threshold values $a = 0.3$ and $b = 0.2$ where used. Finally, in agreement with the previous analysis, the map in Fig. (11 (c)), for which $a = 0.15$ and $b = 0.30$, has the homoclinic topology. We have numerically tested the reconnection threshold Eq. (A4); for small values of a and b the reconnection process is clearly observed, as shown in Fig. (11). For large parameter values, the map exhibits widespread stochasticity and the concept of reconnection has no visible meaning. For intermediate parameter values, the stochastic layer of the primary islands is visible and so it would be more appropriate to refer to this process as *stochastic layer reconnection.* If we apply the reconnection criterion of Eq. (A4) to the map of Eqs.(64) and (65), we get as expected the heteroclinic topology, which is appropriate for modelling transport by waves in the presence of a shear flow. On the other had, the criterion implies that the topology of the traveling wave map [13] will always be homoclinic.

References

[1] J. Pedlosky, *Geophysical Fluid Dynamics*, 2nd Ed. (Springer-Verlag, New York, 1987).

[2] R.S. MacKay and J.D. Meiss (eds.), *Hamiltonian Dynamical Systems: a reprint selection* (Adam-Hilger, London, 1987).

[3] H. Aref, Stirring by Chaotic Advection, J. Fluid Mech. **143**, 1 (1984).

[4] J. Chaiken, R. Chevray, M. Tabor, and Q.M. Tan, Experimental Study of Lagrangian Turbulence in Stokes Flow, Proc. R. Soc. London, Ser. A, **408**, 165 (1986).

[5] J.M. Ottino, Mixing, Chaotic Advection and Turbulence, Ann. Rev. Fluid Mech. **22** 207 (1990).

[6] D. del-Castillo-Negrete and P.J. Morrison, Hamiltonian Chaos and Transport in Quasi-geostrophic Flows, *Research Trends in Physics*: Chaotic Dynamics and Transport in Fluids and Plasmas, eds. I. Prigogine, *et al.*, AIP, 1991, in press.

[7] B.V. Chirikov, A Universal Instability of Many-Dimensional Oscillator Systems, Phys. Reports **52**, 5, 263 (1979).

[8] A.J. Lichtenberg and M.A. Lieberman, *Regular and Stochastic Motion* (Springer-Verlag, New York, 1983).

[9] J. Sommeria, S.D. Meyers, and H.L. Swinney, Laboratory Model of a Planetary Eastward Jet, Nature **337**, 58 (1989).

[10] J. Sommeria, S.D. Meyers, and H.L. Swinney, Experiments on Vortices and Rossby Waves in Eastward and Westward Jets; *Nonlinear Topics in Ocean Physics*, ed. A. Osborne (North-Holland, Amsterdam, 1991).

[11] R.P. Behringer, S.D. Meyers and H.L. Swinney, Chaos and Mixing in a Geostrophic Flow, Phys. Fluids A **3**, 5, 1243 (1991).

[12] L.M. Polvani and S. Touma, A Note on Recent Experiments with Rossby Waves on Eastward Jets; *Nonlinear Phenomena in Atmospheric and Oceanic Sciences*, eds. G. Carnevale and R. Pierrehumbert (Springer-Verlag, New York, 1991).

[13] J.B. Weiss, Transport and Mixing in Traveling Waves, Phys. Fluids A **3**, 5, 1379 (1991).

[14] H.L. Kuo, Dynamic Instability of Two-Dimensional Nondivergent Flow in a Barotropic Atmosphere, J. Met. **6**, 105 (1949).

[15] F.B. Lipps, The Barotropic Stability of the Mean Winds in the Atmosphere, J. Fluid Mech. **12**, 397 (1962).

[16] R.T. Pierrehumbert, Chaotic Mixing of Tracer and Vorticity by Modulated Traveling Rossby Waves, Geophys. Astrophys. Fluid Dynamics, **58**, 285, 1991.

[17] T. Solomon, W. Holloway, and H. Swinney (private communication).

[18] S.D Meyers, Cross-Frontal Mixing in a Meandering Jet, submitted to J. Phys. Oceanogr., Feb. 1992.

[19] J.E. Howard and S.M. Hohs, Stochasticity and Reconnection in Hamiltonian Systems, Phys. Rev. Lett. **29**, 1, 418 (1989).

Figure Captions

1. Phase space for Hamiltonian (56) with $\varepsilon_2 = 0.3$ and $\beta = 0.614$. This is the phase space topology of a general Hamiltonian representing the propagation of a linear Rossby wave in a symmetric shear flow.

2. Depiction of isolated resonance pairs used in the overlap criterion. Banded chaos occurs when the resonance at y_1^* overlaps that at y_2^* and simultaneously because of symmetry $-y_1^*$ and $-y_2^*$ overlap. An estimate for global chaos is given by the overlap of y_2^* with $-y_1^*$.

3. Iterations of the area preserving map of (48) and (49) for $a = 0.5$ and $b = 0.125$.

4. Distances between the resonances as a function of beta. The distance between resonances y_2^* and $-y_1^*$ in Fig. 2 is given by d_+, while d_- gives the distance between y_2^* and y_1^*.

5. Poincáre section of Hamiltonian (55) with $\varepsilon_1 = 0.1$, $\varepsilon_2 = 0.3$, and increasing values of β: (a) $\beta = 0.186$, (b) $\beta = 0.317$, and (c) $\beta = 0.614$. The spatial periods of the system in the x-direction are $D = 22.9$, 16.9, and 15.7 for cases (a), (b), and (c), respectively. For a clearer visualization in (a) and (b) we only displayed points in the region $x \in (0, D/2)$ and in (c) only points with $x \in (0, D/3)$.

6. Potential vorticity of the zonal flow for $\beta = 0.614$, the same value used in the Poincáre section of Fig. 5(c). The potential vorticity is flat; i.e. nearly constant, in the regions where the bands of chaotic transport lie in the Poincáre section, indicating the consistent co-existence of chaotic transport and potential vorticity conservation. At the same time, the robustness of the central barrier in the Poincáre section is related to the sharp potential vorticity gradient near $y = 0$.

7. Stochasticity in the area preserving map of (64) and (65) for $a = 1.5$ in case (a) and $a = 2.8$ in case (b). In case (a) banded chaos with trapping regions appears, while in case (b) these regions have been destroyed. By comparing these plots with Figs. 5(b) and 5(c) we see that the map reproduces qualitatively the topology and transport properties of the continuous Hamiltonian system (51).

8. Cross-section of the rotating annulus used by Sommeria *et al.* [9], [10] for experiments on dynamics and transport by Rossby waves. The annulus has an inner radius of 10.8 cm and an outer radius of 43.2 cm. The depth of the tank increases from 17.1 cm at the inner radius to 20.3 cm at the outer radius, resulting in a conical bottom topography with slope equal to -0.1. The entire tank rotates at a constant angular velocity in the range from 0 to 25 rad/sec. Fluid is pumped through ports located in the bottom of the tank, the arrow indicates the pattern of inlets (I) and outlets (0). The radial distance between ports is 8.1 cm (after Sommeria *et al.* [10]).

9. (a) Contour plot of the stream function deduced from a particle streak photograph of the flow (after Behringer *et al.* [11]). (b) Phase space of Hamiltonian (63) at a fixed time with parameters $A = 12\,\text{cm/sec}$, $r_0 = 25\,\text{cm}$, $L = 6.4\,\text{cm}$, $m_1 = 6$, $m_2 = 5$, $\omega_1 = 1.162\,\text{rad/sec}$, $\omega_2 = 0.632\,\text{rad/sec}$, $\beta = 0.64$, $\varepsilon_1 = 0.1$ and $\varepsilon_2 = 0.3$.

10. Poincáre section obtained by fourth order Runge-Kutta integration of the Hamiltonian system (63), with parameters $A = 12\,\text{cm/sec}$, $r_0 = 25\,\text{cm}$, $L = 6.4\,\text{cm}$, $m_1 = 6$, $m_2 = 5$, $\omega_1 = 1.162\,\text{rad/sec}$, $\omega_2 = 0.632\,\text{rad/sec}$, $\beta = 0.64$, $\varepsilon_1 = 0.1$, and $\varepsilon_2 = 0.3$ for case (a) and $\varepsilon_1 = 0.03$ for case (b). The stability islands observed in case (b) are trapping regions.

11. Separatrix reconnection in the standard non-twist map of (A1) and (A2). In case (a) $a = 0.5$ and $b = 0.1$. The map exhibits an heteroclinic type topology. Case (b)

corresponds to the reconnection threshold $a = 0.3$ and $b = 0.2$. In case (c) the values $a = 0.15$ and $b = 0.3$ give an homoclinic type topology.

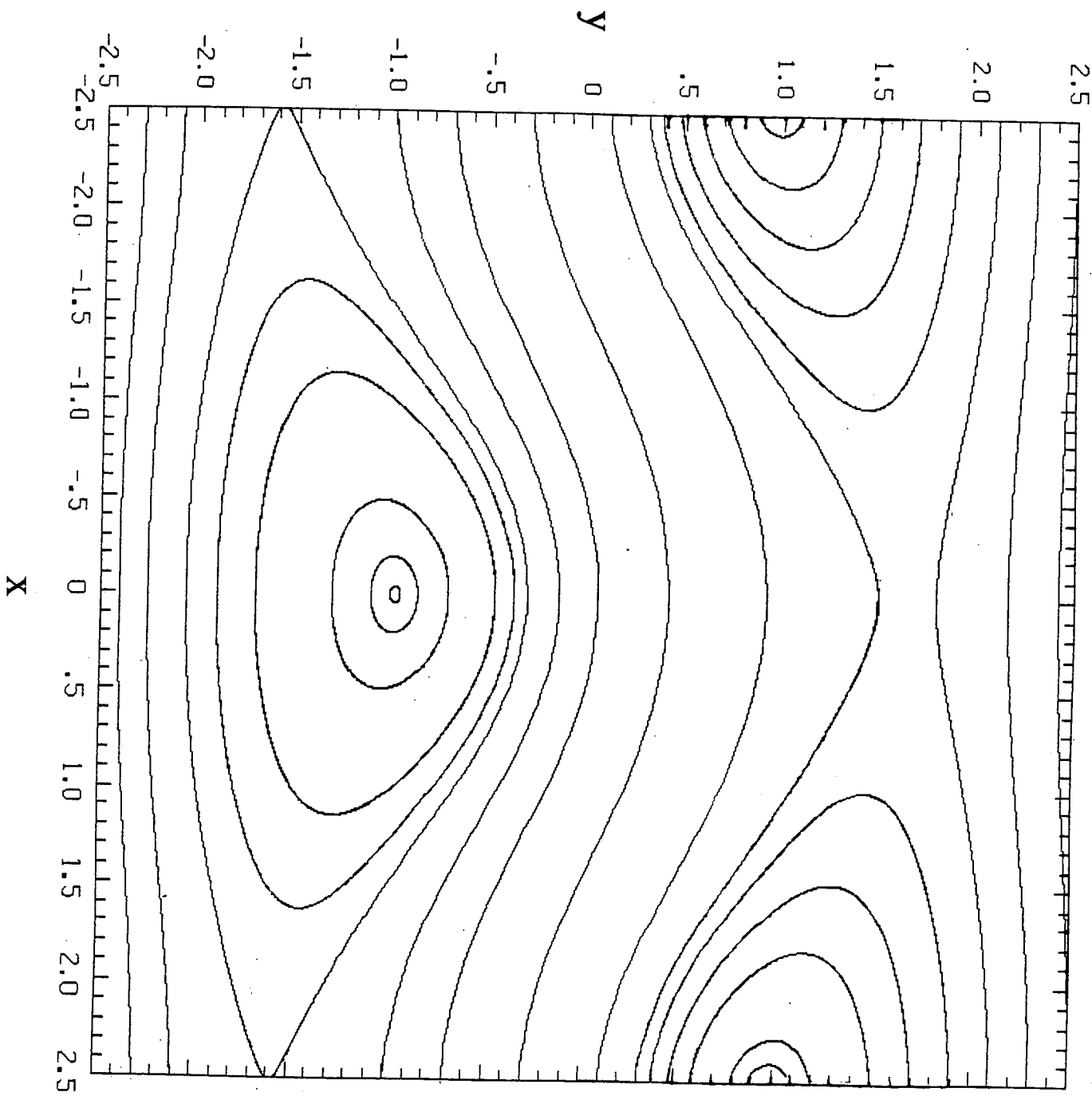

Figure 1

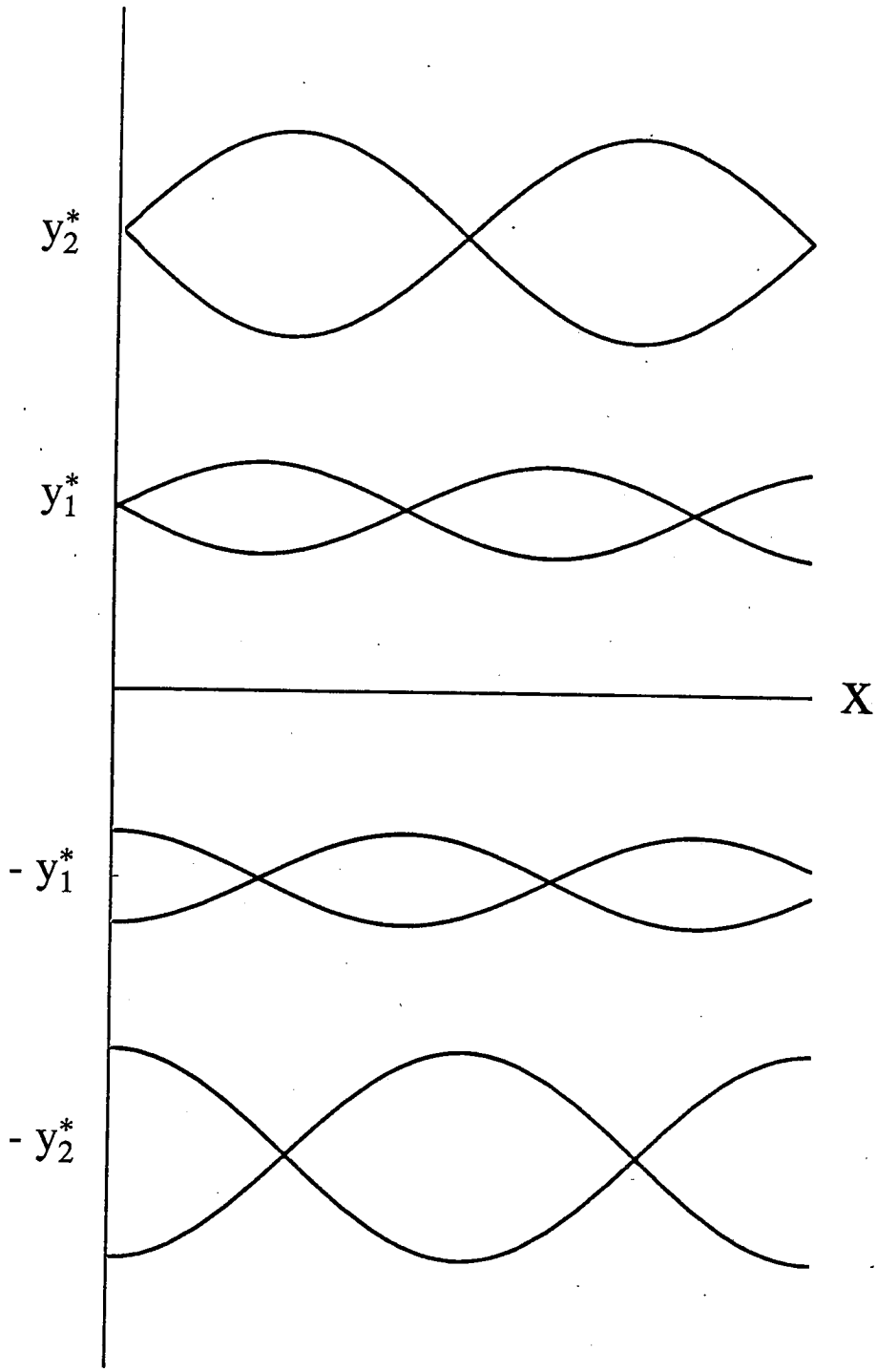

Figure 2

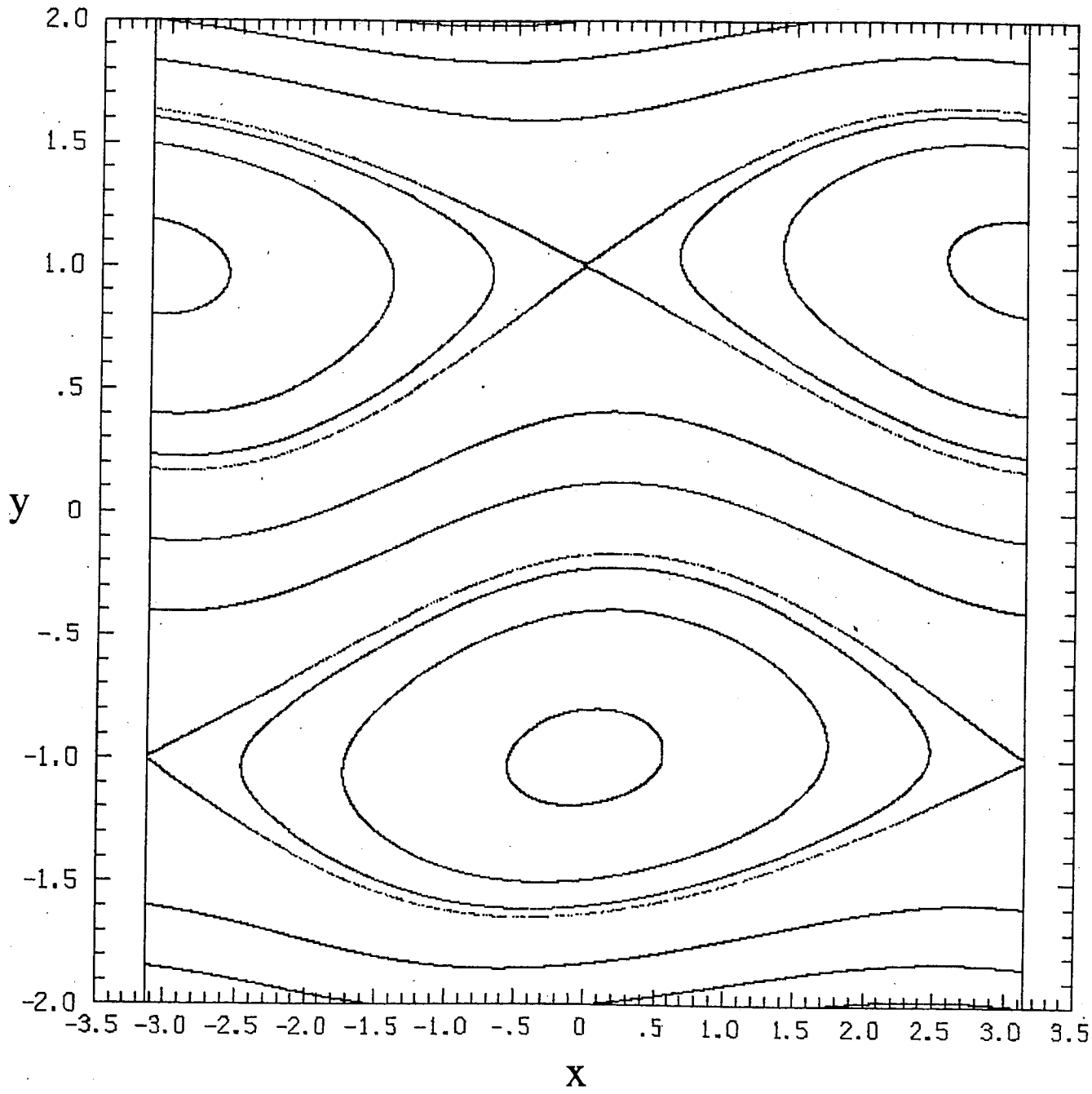

Figure 3

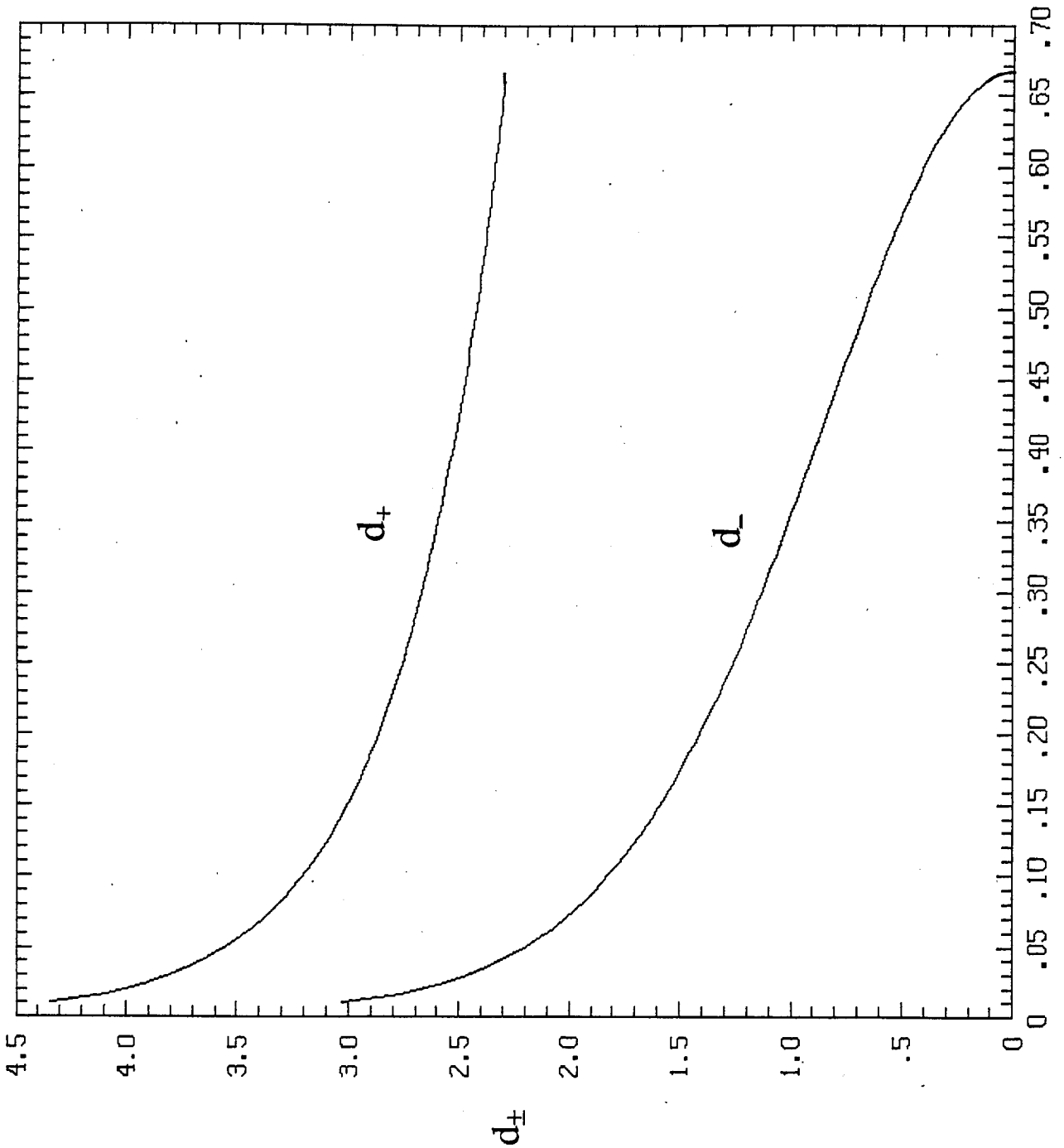
4.5
4.0
3.5
3.0
2.5
2.0
1.5
1.0
.5
0
$d_{\pm}$
d_+
d_-
0
.05
.10
.15
.20
.25
.30
.35
.40
.45
.50
.55
.60
.65
.70
β

Figure 4

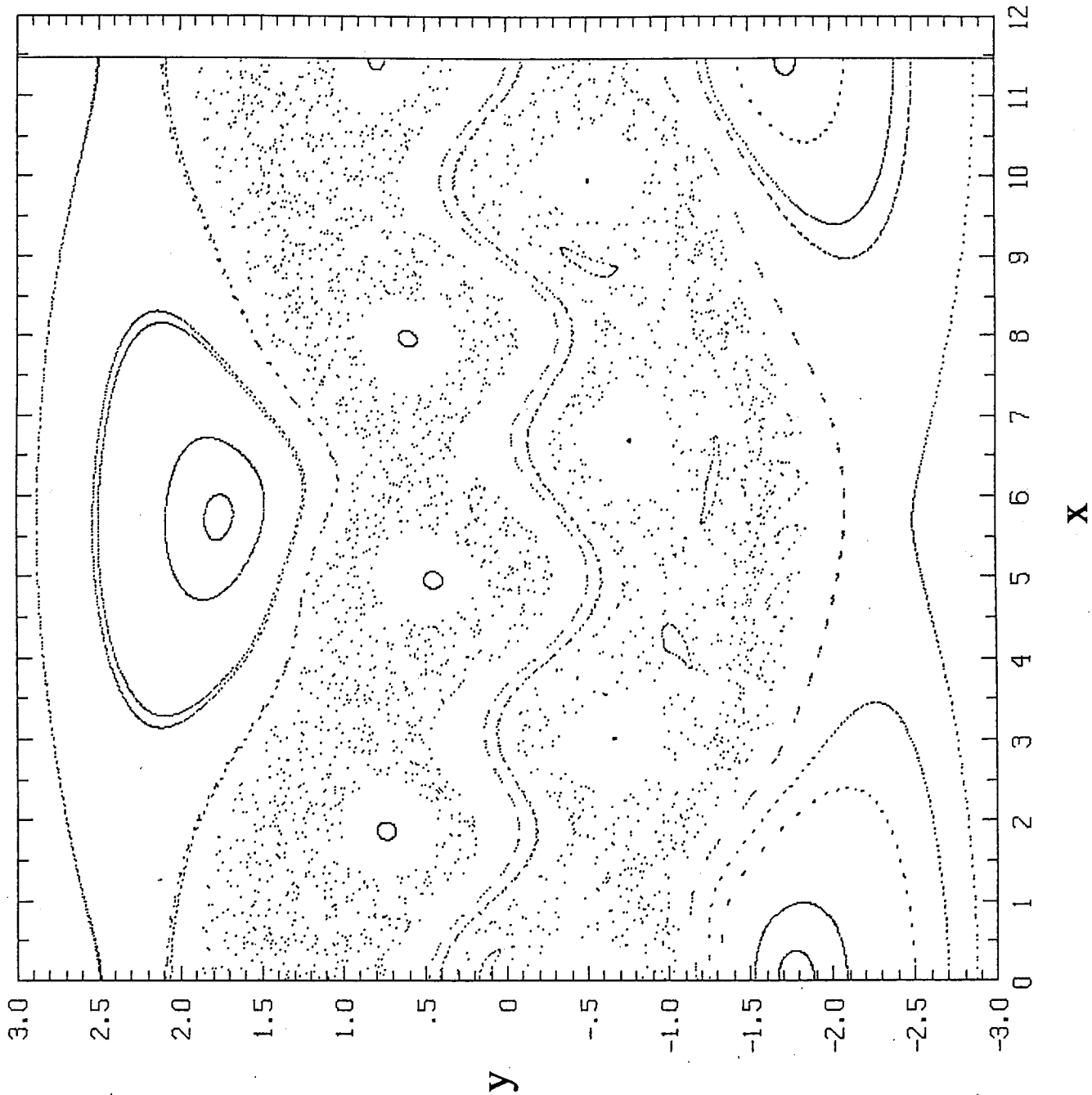

Figure 5(a)

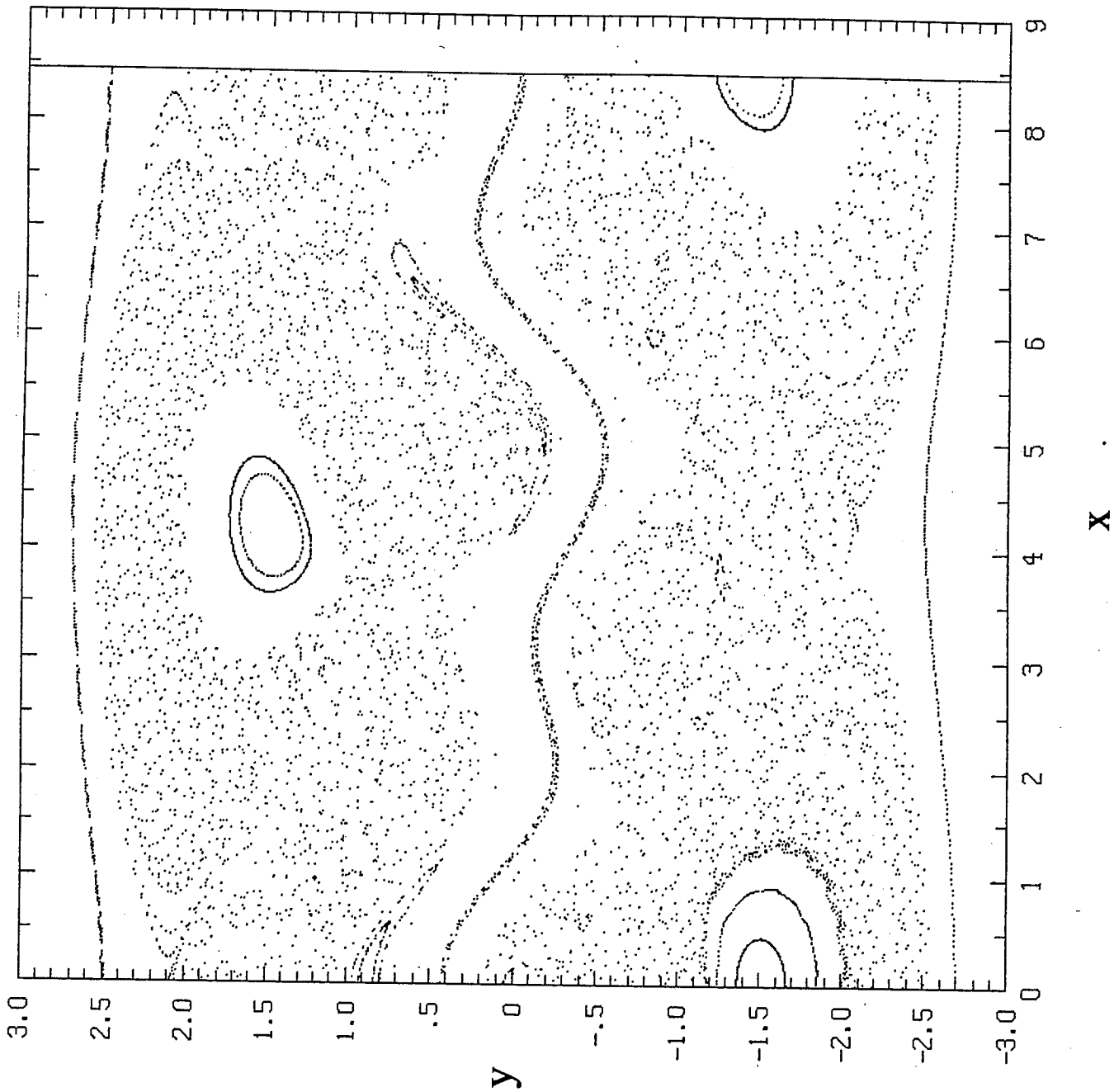

Figure 5(b)

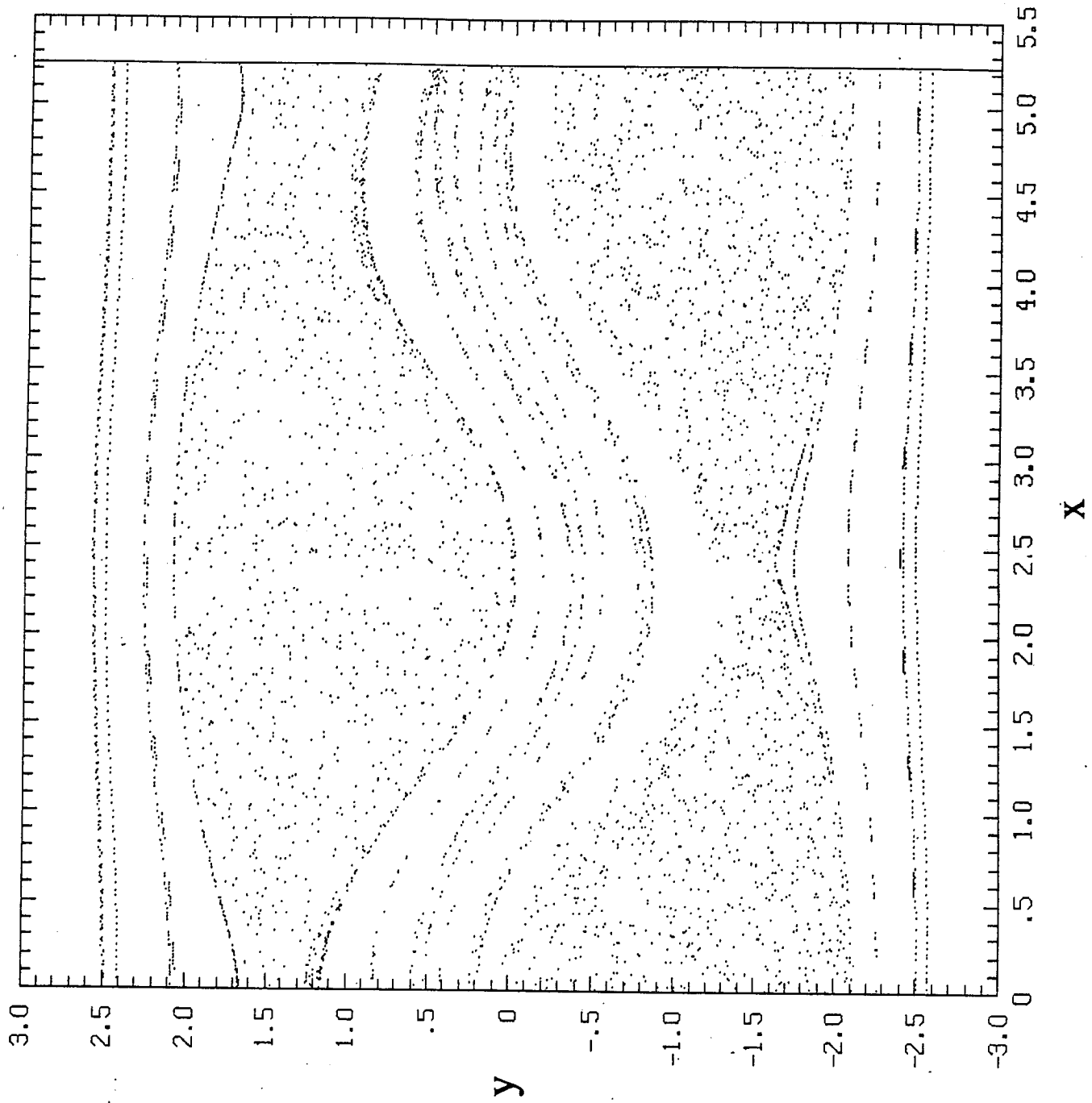

Figure 5(c)

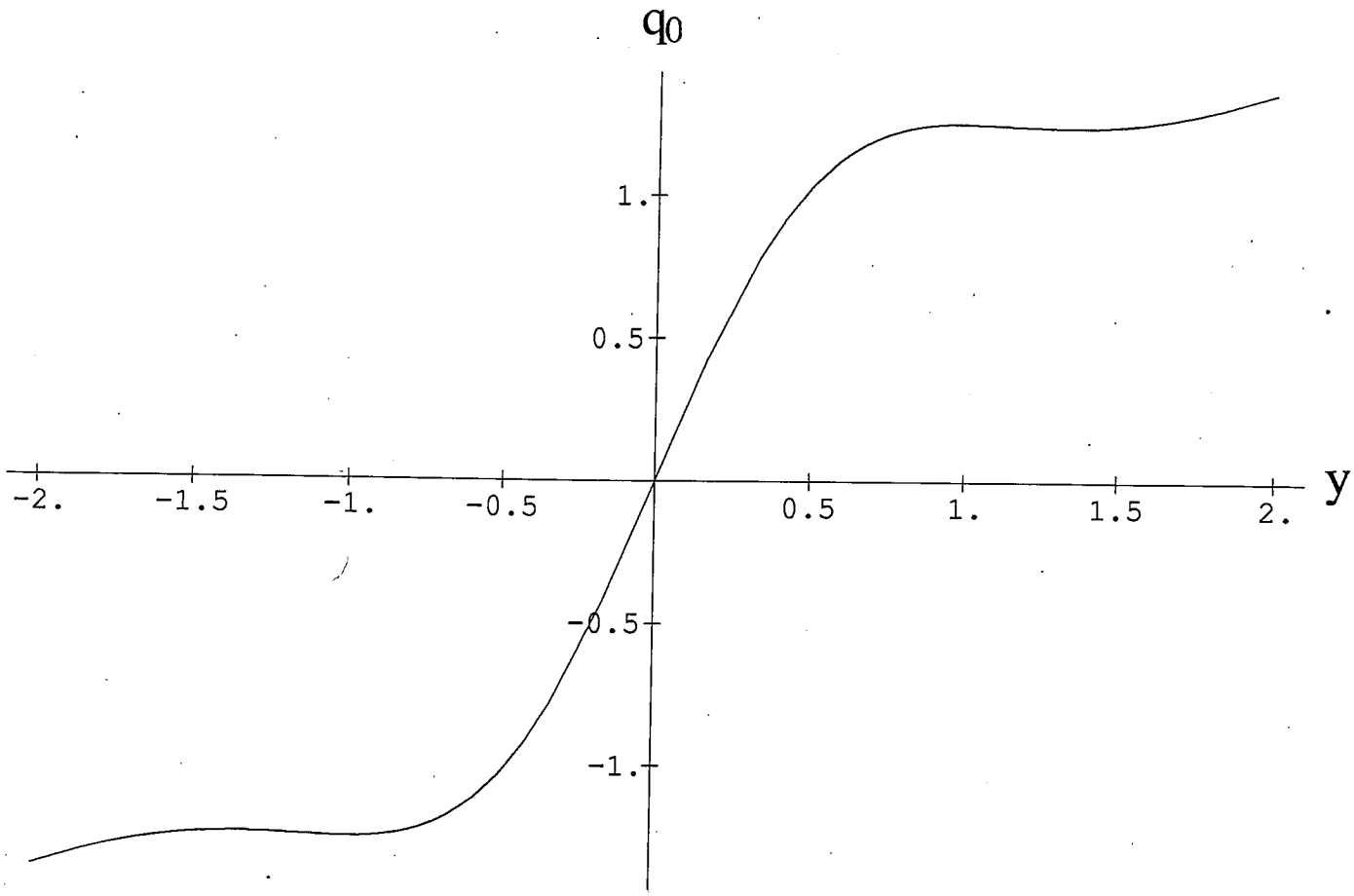

Figure 6

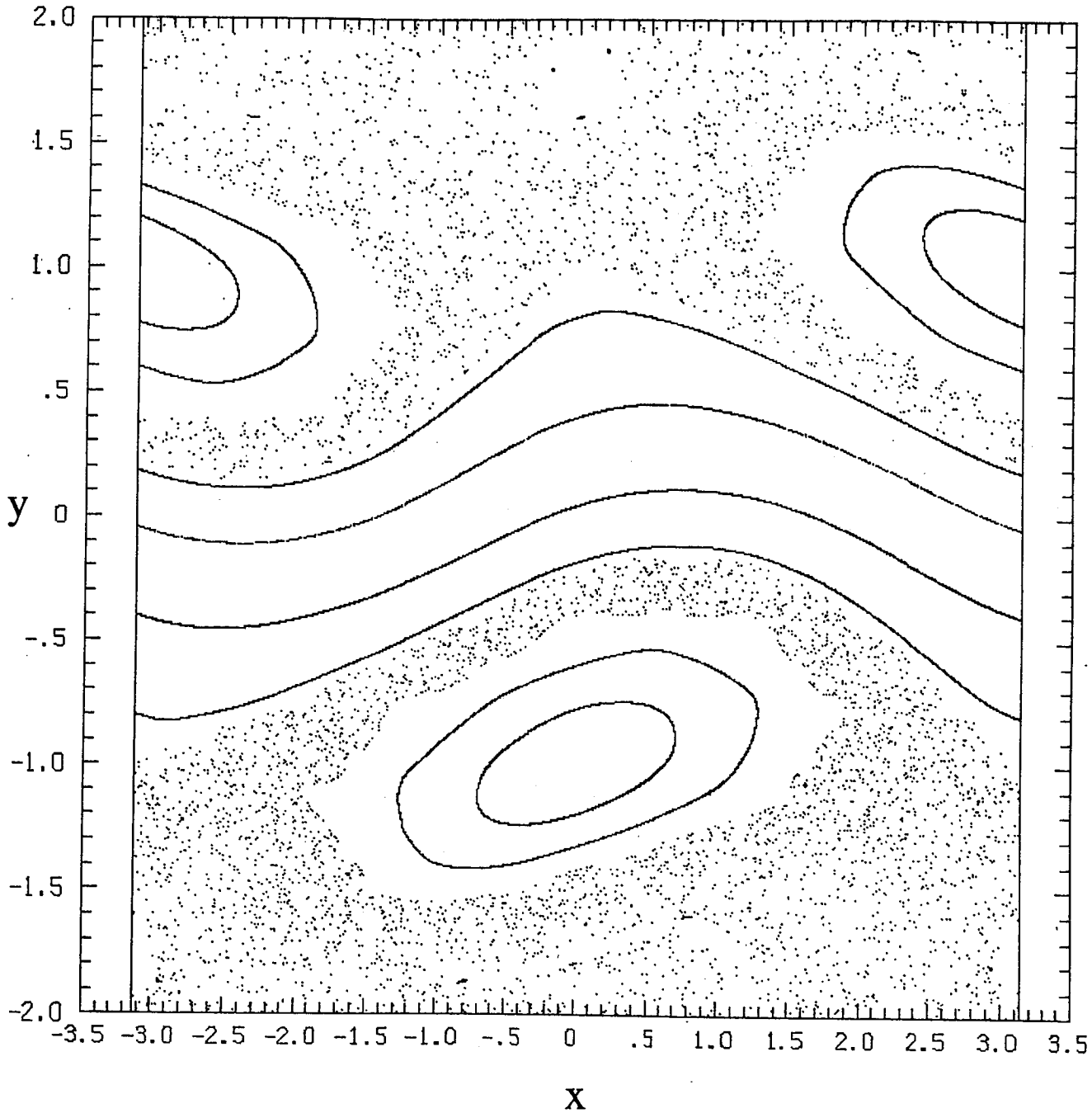

Figure 7(a)

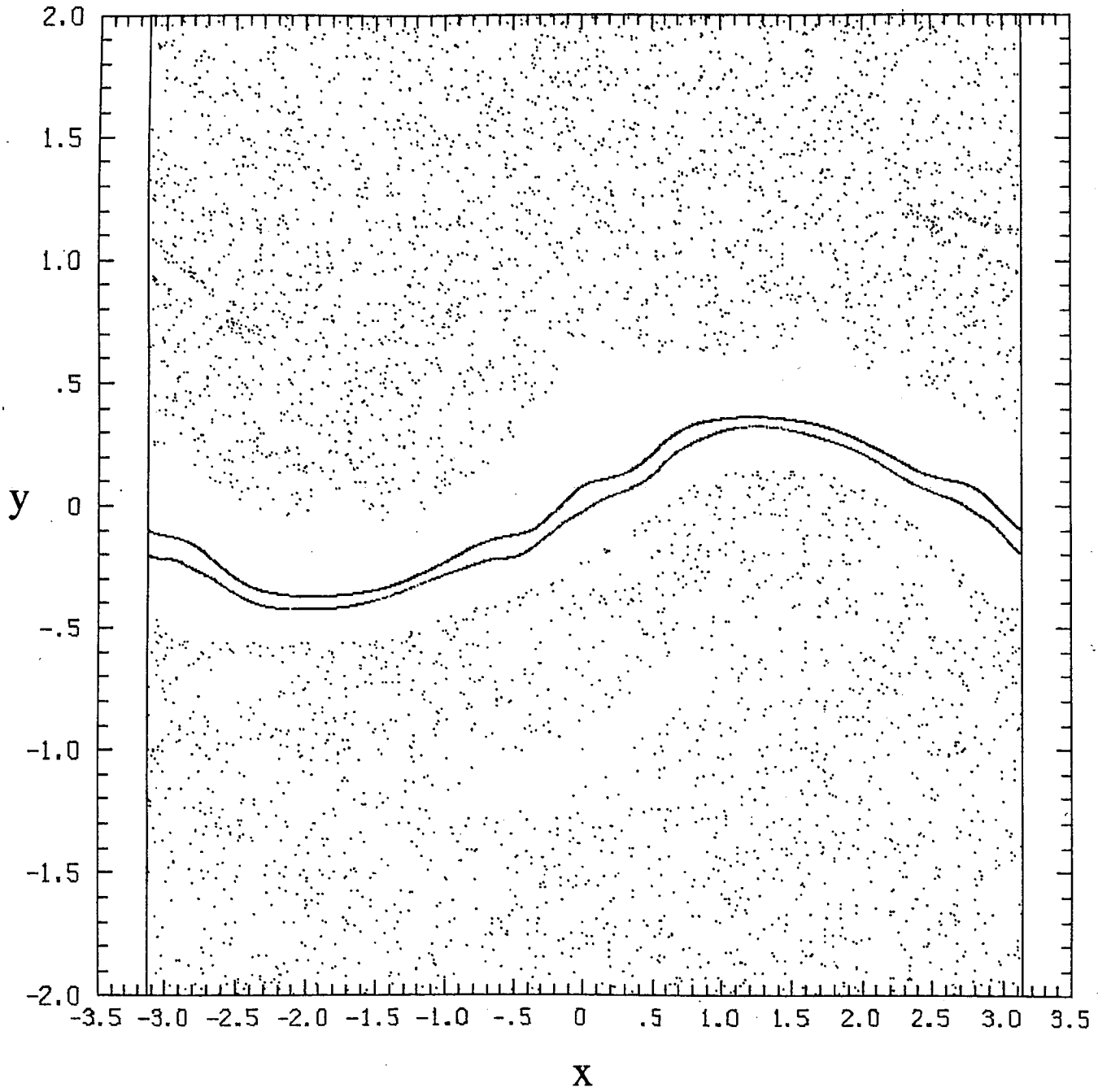

Figure 7(b)

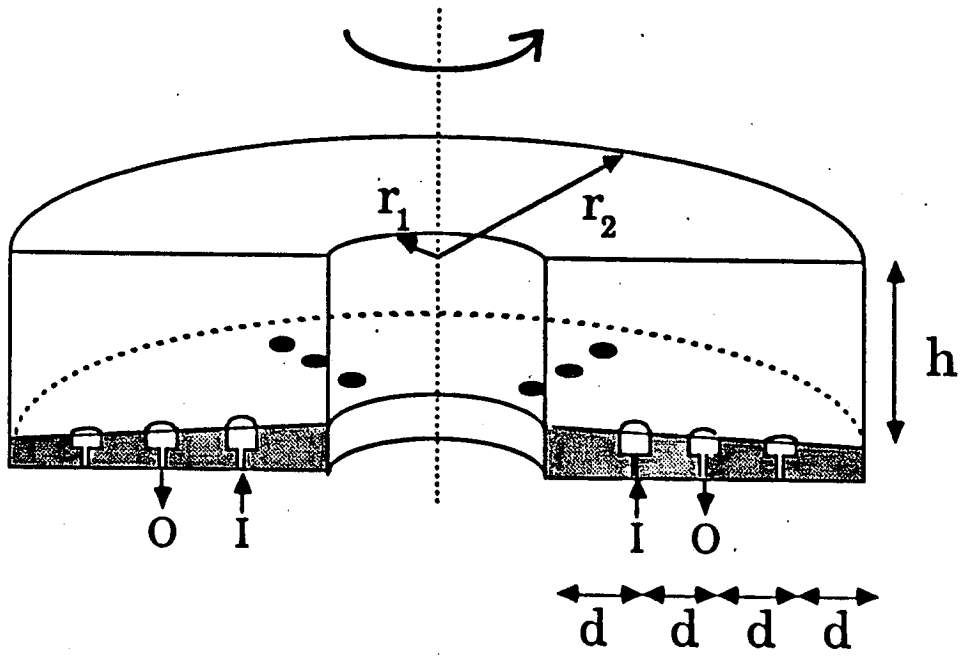

Figure 8

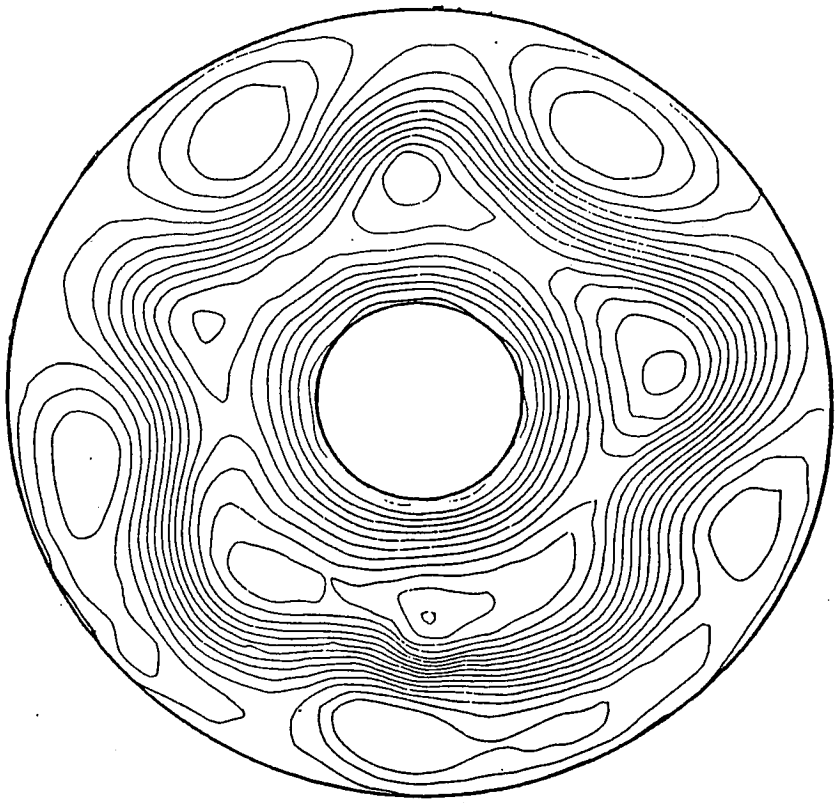

Figure 9(a)

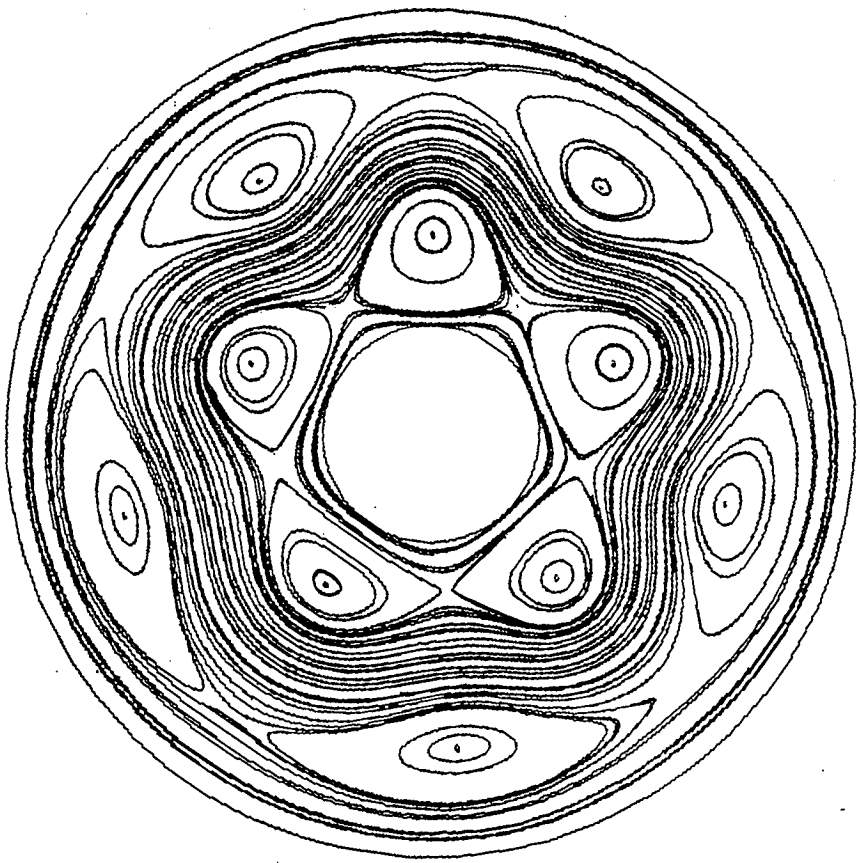

Figure 9(b)

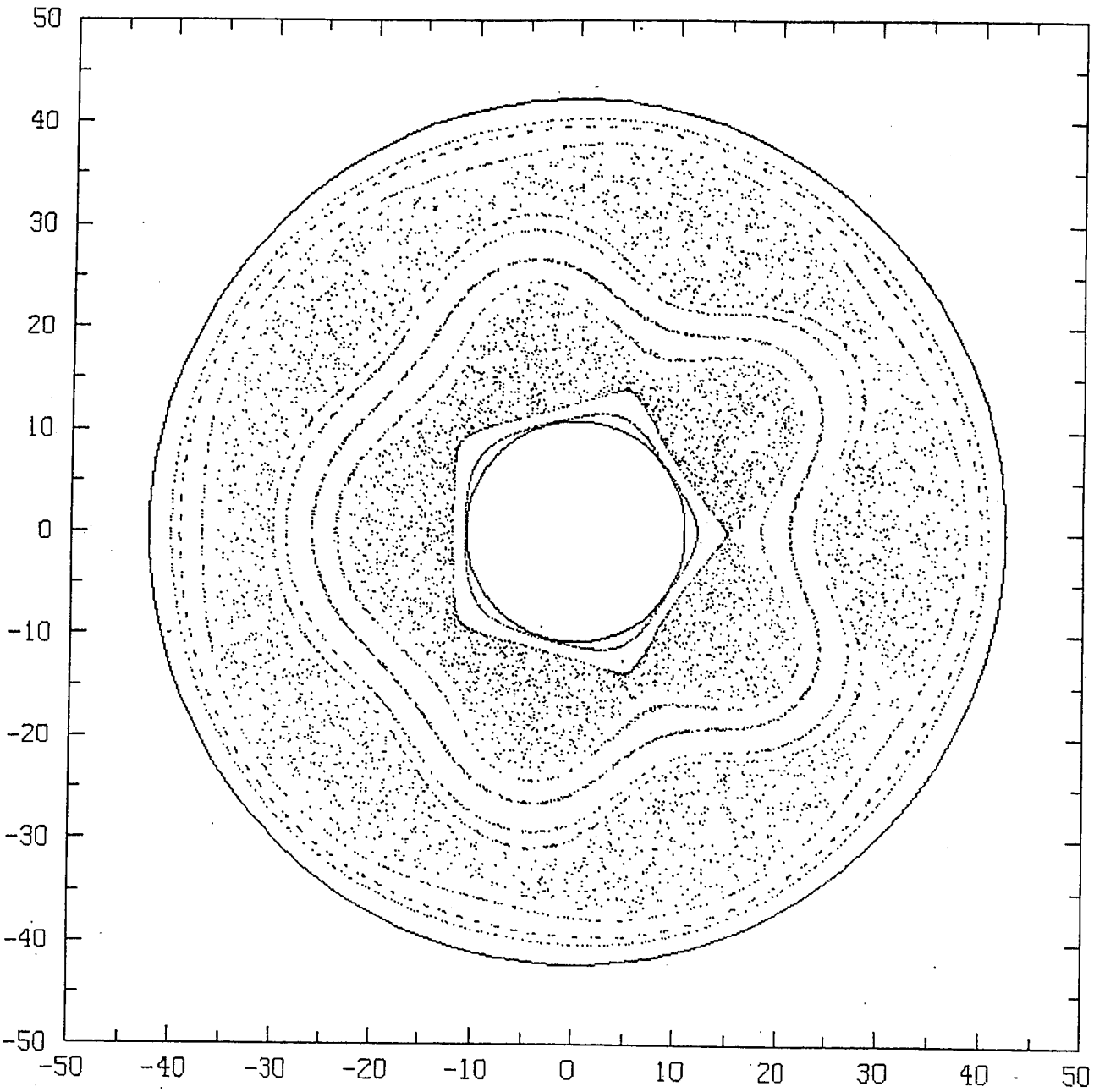

Figure 10(a)

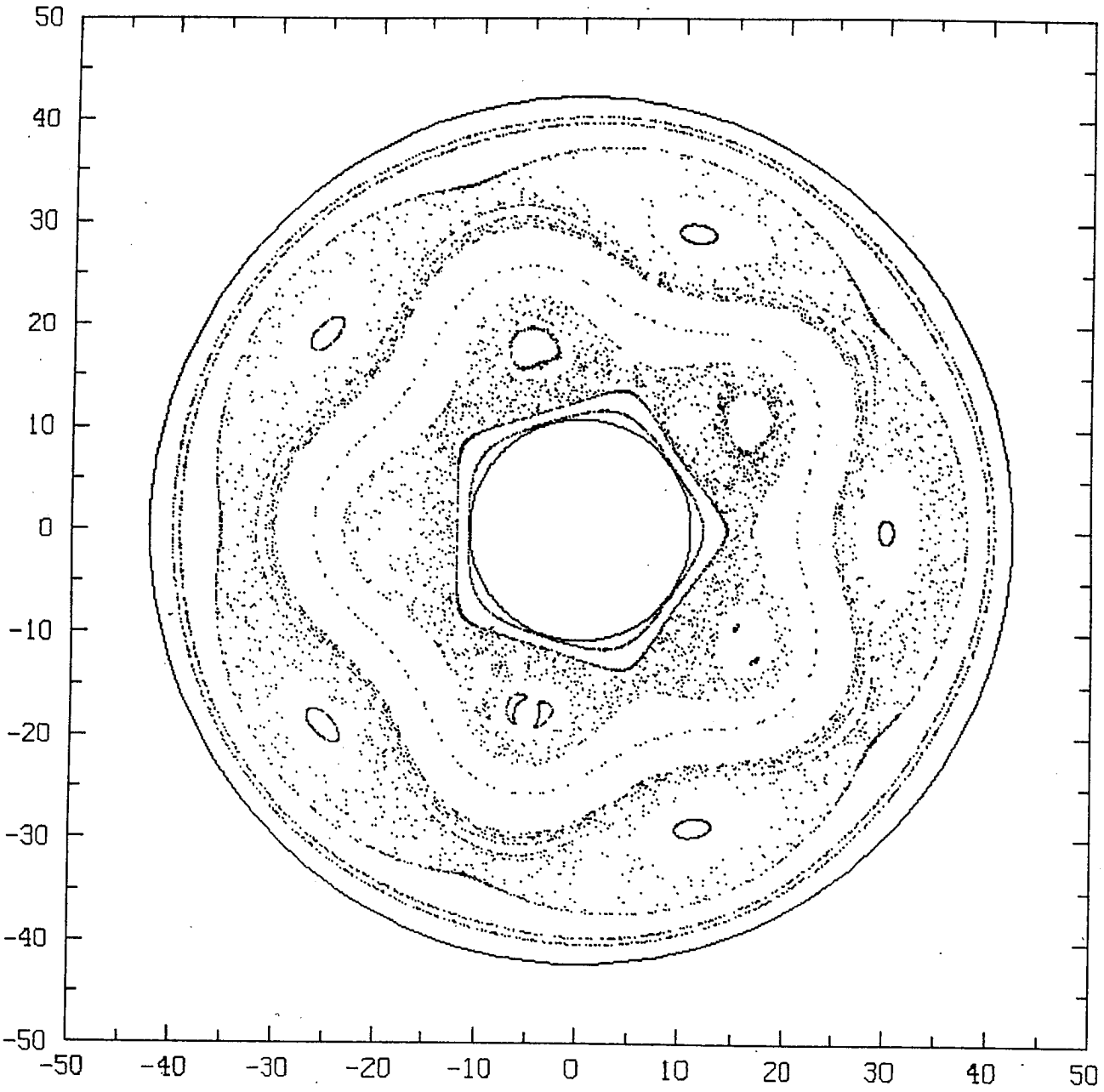

Figure 10(b)

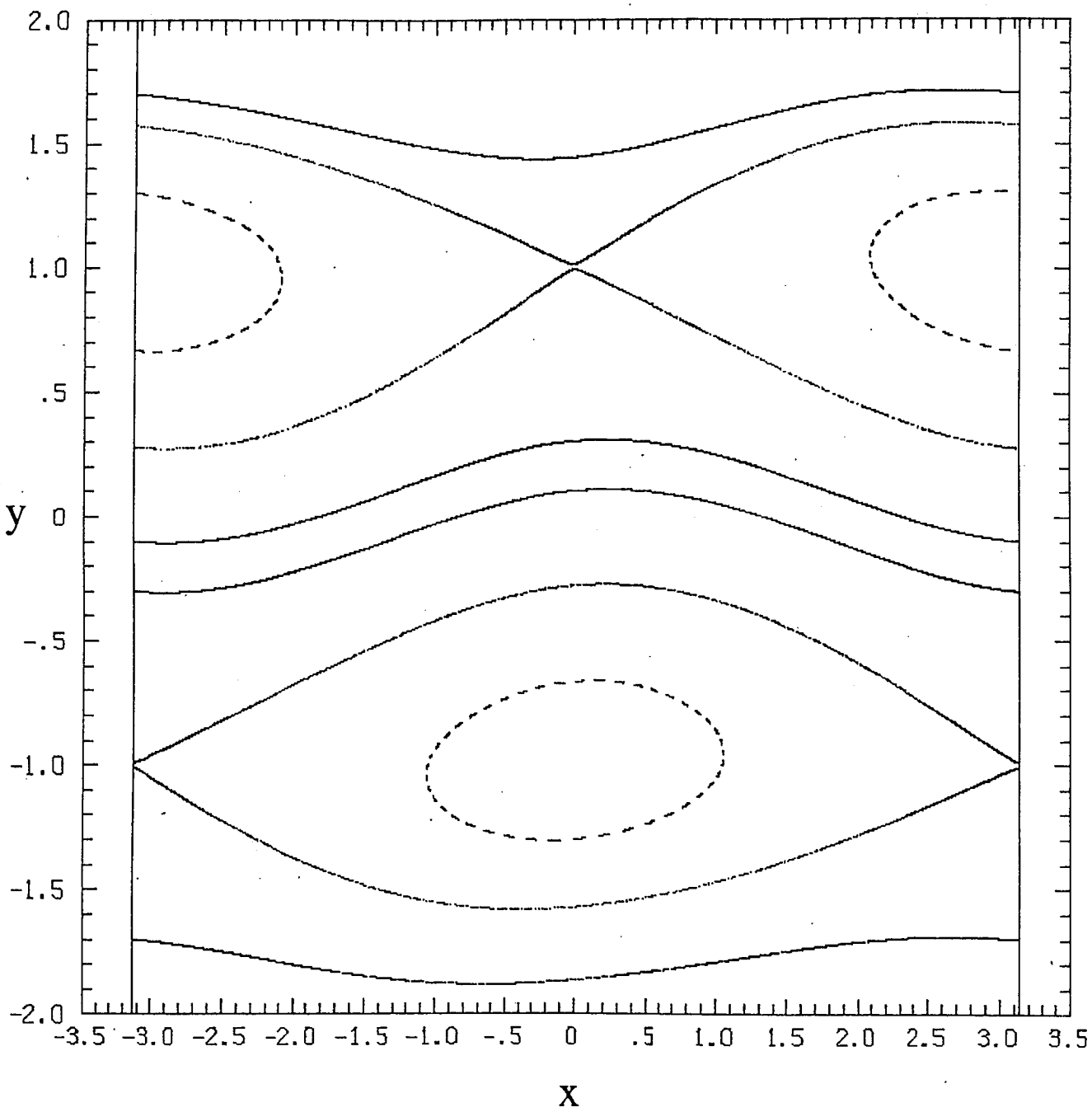

Figure 11(a)

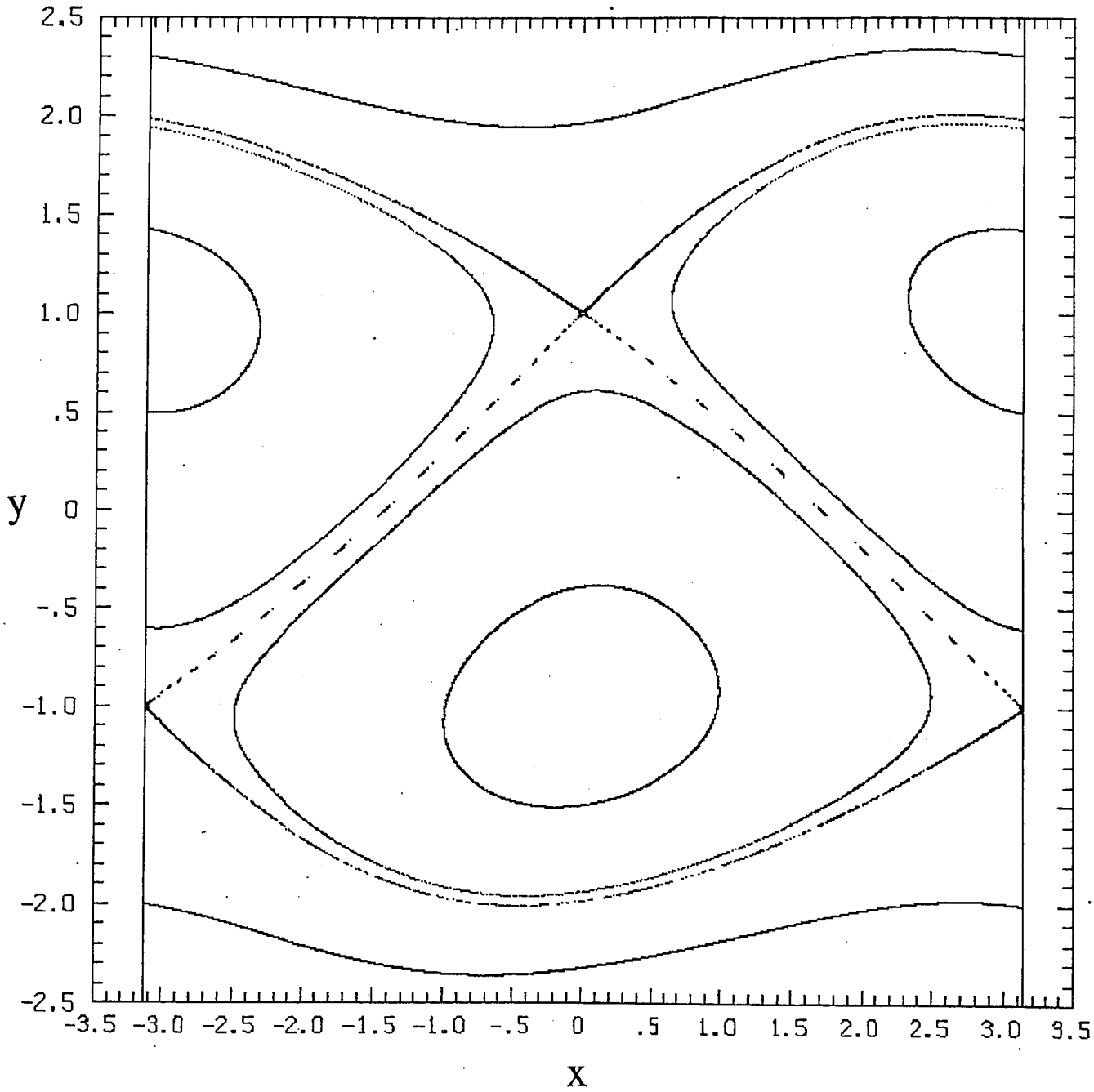

Figure 11(b)

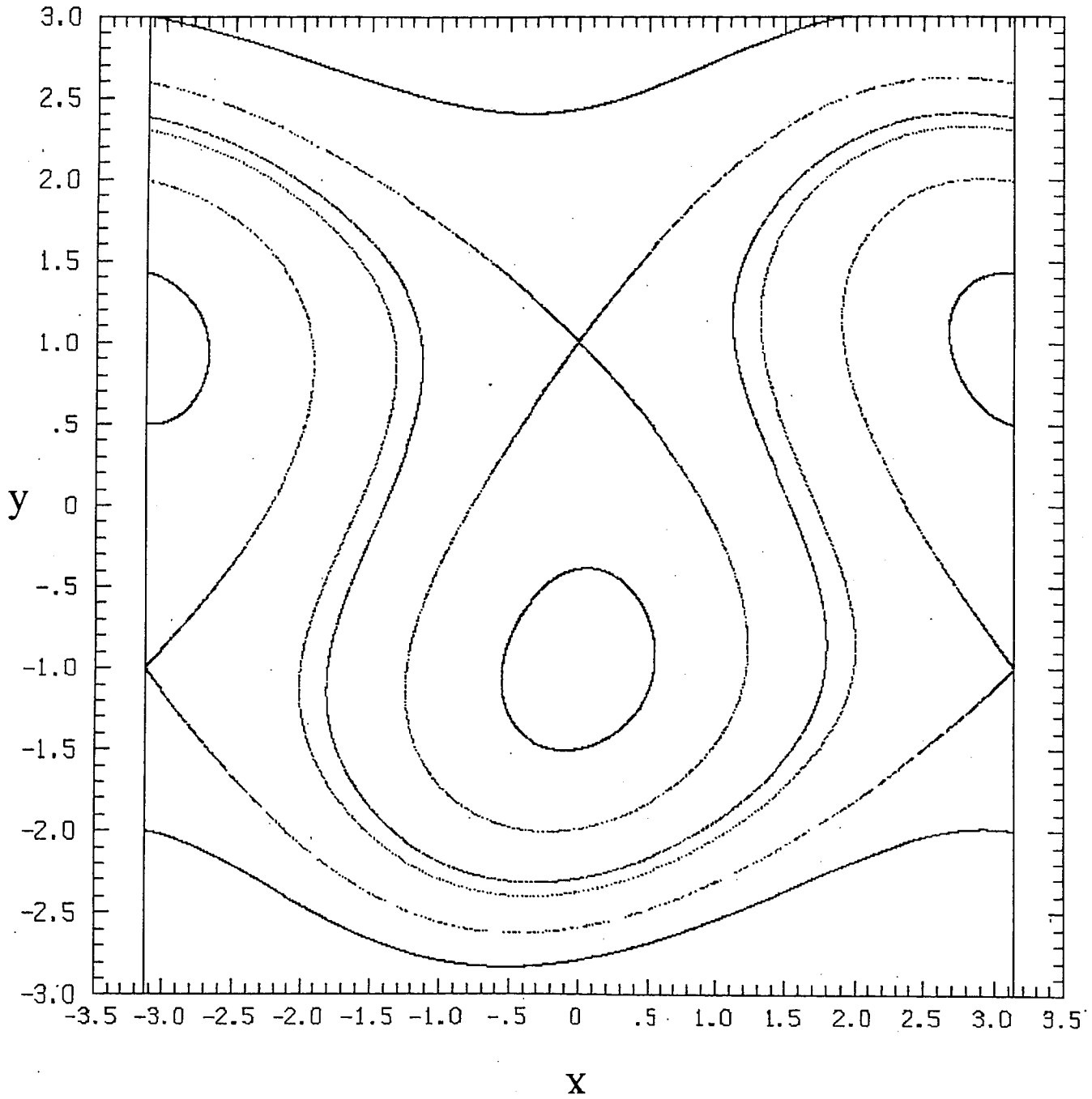
3.0
2.5
2.0
1.5
1.0
.5
y 0
-.5
-1.0
-1.5
-2.0
-2.5
-3.0
-3.5 -3.0 -2.5 -2.0 -1.5 -1.0 -.5 0 .5 1.0 1.5 2.0 2.5 3.0 3.5
x

Figure 11(c)